

Impact of grids and dynamical cores in CESM2.2 on the surface mass balance of the Greenland Ice Sheet

Adam R. Herrington¹, Peter H. Lauritzen¹, Marcus Lofverstrom², William H. Lipscomb¹, Andrew Gettelman¹ and Mark A. Taylor³

¹National Center for Atmospheric Research, 1850 Table Mesa Drive, Boulder, Colorado, USA

²Department of Geosciences, University of Arizona, 1040 E. 4th Street, Tucson, Arizona USA

³Sandia National Laboratories, Albuquerque, New Mexico, USA

Key Points:

- The CESM2.2 release includes several enhancements to the spectral-element dynamical core, including two new Arctic refined mesh configurations.
- Uniform resolution grids degrade the surface mass balance of the Greenland Ice Sheet compared with equivalent low resolution latitude-longitude grids.
- The refined Arctic meshes substantially improve the surface mass balance over all low resolution grids.

15 **Abstract**

16 Six different configurations, a mixture of grids and atmospheric dynamical cores
 17 available in the Community Earth System Model, version 2.2 (CESM2.2), are evaluated
 18 for their skill in representing the climate of the Arctic and the surface mass balance of
 19 the Greenland Ice Sheet (GrIS). The conventional 1° – 2° uniform resolution grids sys-
 20 tematically overestimate both accumulation and ablation over the GrIS. Of these con-
 21 ventional grids, the latitude-longitude grids outperform the quasi-uniform unstructured
 22 grids owing to their higher degrees of freedom in representing the GrIS. Two Arctic-refined
 23 meshes, with $1/4^{\circ}$ and $1/8^{\circ}$ refinement over Greenland, are documented as newly sup-
 24 ported configurations in CESM2.2. The Arctic meshes substantially improve the sim-
 25 ultated clouds and precipitation rates in the Arctic. Over Greenland, these meshes skill-
 26 fully represent accumulation and ablation processes, leading to a more realistic GrIS sur-
 27 face mass balance. As CESM is in the process of transitioning away from conventional
 28 latitude-longitude grids, these new Arctic refined meshes improve the representation of
 29 polar processes in CESM by recovering resolution lost in the transition to quasi-uniform
 30 grids.

31 **1 Introduction**

32 General Circulation Models (GCMs) are powerful tools for understanding the me-
 33 teorology and climate of the high latitudes, which are among the most sensitive regions
 34 on Earth to global and environmental change. GCMs differ vastly in their numerical treat-
 35 ment of polar regions because of the so-called *pole-problem* (Williamson, 2007). The pole
 36 problem refers to numerical instability arising from the convergence of meridian lines into
 37 polar singularities on latitude-longitude grids (e.g., Figure 1a, hereafter referred to as
 38 *lat-lon* grids). Depending on the numerics, methods exist to suppress this instability, and
 39 lat-lon grids may be advantageous for polar processes by representing structures with
 40 finer resolution than elsewhere in the computational domain. With the recent trend to-
 41 wards globally uniform unstructured grids, any potential benefits of lat-lon grids in po-
 42 lar regions may be lost. In this study, we evaluate a number of grids and dynamical cores
 43 (hereafter referred to as *dycores*) available in the Community Earth System Model, ver-
 44 sion 2.2 (CESM2.2; Danabasoglu et al., 2020), including new variable-resolution grids,
 45 to understand their impacts on the simulated Arctic climate. We focus specifically on
 46 the climate and surface mass balance of the Greenland Ice Sheet.

47 In the 1970s, the pole problem was largely defeated through the adoption of effi-
 48 cient spectral transform methods in GCMs (see Williamson, 2007, and references therein).
 49 These methods transform grid point fields into a global, isotropic representation in wave
 50 space, where linear operators (e.g., horizontal derivatives) in the (truncated) equation
 51 set can be solved exactly. While spectral transform methods are still used today, local
 52 numerical methods have become desirable for their ability to run efficiently on massively
 53 parallel systems. The pole problem has thus re-emerged in contemporary climate mod-
 54 els that use lat-lon grids, and some combination of reduced grids (modified lat-lon grids,
 55 with cells elongated in the longitudinal direction over the polar regions) and polar fil-
 56 ters are necessary to ameliorate this numerical instability (Jablonowski & Williamson,
 57 2011). Polar filters subdue the growth of unstable computational modes by applying ad-
 58 ditional damping to the numerical solution over polar regions. This damping reduces the
 59 effective resolution in polar regions such that the resolved scales are *approximately* the
 60 same everywhere on the grid. We emphasize *approximately*, since it is at least conceiv-
 61 able that marginal increases in effective resolution occur over polar region in lat-lon grids,
 62 despite polar filtering, since resolved waves can be represented with more grid points than
 63 at lower latitudes.

64 Dycores built on lat-lon grids have some advantages over unstructured grids. Lat-
 65 lon coordinate lines are orthogonal, and aligned with zonally symmetric circulations that

characterize many large-scale features of Earth's atmosphere. Lauritzen et al. (2010) has experimented with rotating lat-lon models such that their coordinate lines no longer align with an idealized, zonally balanced circulation. For the finite-volume lat-lon dycore considered in this paper (hereafter *FV*), numerical errors were shown to be largest when the polar singularity is rotated into the baroclinic zone (45°N latitude), generating spurious wave growth much earlier in the simulation than for other rotation angles. This illustrates the advantages of coordinate surfaces aligned with latitude bands, albeit an extreme example where the polar singularity and the polar filter are also contributing to the spurious wave growth. The unstructured grids all generate spurious baroclinic waves earlier on in the simulations than the (unrotated) lat-lon models, although the unstructured model considered in this paper, the spectral-element dycore (hereafter *SE*), holds a balanced zonal flow without spurious wave growth appreciably longer than the rotated FV experiments (Lauritzen et al., 2010). And unlike *FV*, the *SE* dycore has the same error characteristics regardless of how the grid is rotated.

The polar filter in the *FV* model impedes efficiency at large processor (CPU) counts because it requires a spectral transform, which have large communication overhead (Suarez & Takacs, 1995; Dennis et al., 2012). Unstructured grids support quasi-uniform grid spacing globally, and there is no pole-problem (e.g., Figure 1c). Conversely, unstructured grids are becoming increasingly common due to their improved performance on massively parallel systems and lack of constraints on grid structure (Taylor et al., 1997; Putman & Lin, 2007; Wan et al., 2013). This grid flexibility allows for the adoption of variable-resolution grids (e.g., Figure 2; hereafter abbreviated as *VR*), sometimes referred to as regional grid refinement. In principle, grid refinement over polar regions can make up for any loss of resolution in transitioning away from lat-lon grids (e.g., Figure 2). However, local grid refinement comes at the cost of a smaller CFL-limited time step in the refined region; the CFL-condition — short for Courant–Friedrichs–Lewy condition — is a necessary condition for numerical stability when using discrete data in time and space.

It is important to emphasize that the pole-problem is a distinctive feature of the dycore in atmospheric models. Polar filters do not directly interfere with the physical parameterizations, nor do they have any bearing on the surface models; e.g., the land model can take full advantage of the greater number of grid cells in polar regions on lat-lon grids. This is particularly relevant for the surface mass balance of the Greenland Ice Sheet (*SMB*; the integrated sum of precipitation and runoff), which relies on hydrological processes represented in the land model.

The *SMB* of the Greenland Ice Sheet (hereafter *GrIS*) is determined by processes occurring over a range of scales that are difficult to represent in GCMs (Pollard, 2010). *GrIS* precipitation is concentrated at the ice-sheet margins, where steep topographic slopes drive orographic precipitation. The truncated topography used by low resolution GCMs enables moisture to penetrate well into the *GrIS* interior, manifesting as a positive precipitation bias (Pollard & Groups, 2000; van Kampenhout et al., 2018). *GrIS* ablation areas (marginal regions where seasonal melting exceeds the annual mass input from precipitation) are typically less than 100 km wide and are confined to low-lying areas or regions with low precipitation. These narrow ablation zones are not fully resolved in low resolution GCMs, and may further degrade the simulated *SMB*. For example, CESM, version 2.0 (CESM2) underestimates ablation in the northern *GrIS*, leading to unrealistic ice advance when run with an interactive ice sheet component (Lofverstrom et al., 2020).

Regional climate models (RCMs) are commonly relied upon to provide more accurate *SMB* estimates. The limited area domain used by RCMs permits the use of high resolution grids, capable of resolving *SMB* processes, that can skillfully simulate the *GrIS* *SMB* (Box et al., 2004; Rae et al., 2012; Van Angelen et al., 2012; Fettweis et al., 2013; Mottram et al., 2017; Noël et al., 2018). However, unlike GCMs, RCMs are not a freely evolving system and the atmospheric state must be prescribed at the lateral boundaries

119 of the model domain. The inability of the RCM solution to influence larger-scale dynamics
 120 outside the RCM domain (due to the prescribed boundary conditions) severely limits this approach from properly representing the role of the GrIS in the climate system.
 121 In addition, the boundary conditions are derived from a separate host model, which introduces
 122 inconsistencies due to differences in model design between the host model and the RCM.
 123

125 In order to retain the benefits of RCMs in a GCM, van Kampenhout et al. (2018)
 126 utilized the VR capabilities of the SE dycore in CESM, generating a grid where Greenland
 127 is represented with $1/4^\circ$ resolution, and elsewhere with the more conventional 1°
 128 resolution. The simulated SMB compared favorably to the SMB from RCMs and obser-
 129 vations. The VR approach is therefore emerging as a powerful tool for simulating and
 130 understanding the GrIS and its response to different forcing scenarios, in the freely evolv-
 131 ing GCM framework.

132 The SE dycore has been included in the model since CESM, version 1, but has been
 133 under active development ever since. This includes the switch to a dry-mass vertical co-
 134 ordinate (Lauritzen et al., 2018) and incorporation of an accelerated multi-tracer trans-
 135 port scheme (Lauritzen et al., 2017), made available in CESM2. This paper documents
 136 several additional enhancements to the SE dycore as part of the release of CESM2.2. These
 137 include three new VR configurations (Figure 2), two Arctic meshes and a Contiguous
 138 United-States mesh (**CONUS**; featured in Pfister et al. (2020)). While there are dozens of
 139 published studies using VR in CESM (e.g., Zarzycki et al., 2014; Rhoades et al., 2016;
 140 Gettelman et al., 2017; Burakowski et al., 2019; Bambach et al., 2021), these studies ei-
 141 ther used development code or collaborated closely with model developers. CESM2.2 is
 142 the first code release that contains out of the box VR functionality in CESM.

143 This study compares the representation of Arctic regions using the SE and FV dy-
 144 cores in CESM2.2 (see description below), as these two dycores treat high latitudes (i.e.,
 145 the pole problem) in different ways. Section 2 documents the grids, dycores, and phys-
 146 ical parameterizations used in this study, and also describes the experiments, datasets,
 147 and evaluation methods. Section 3 analyzes the results of the experiments, and Section 4
 148 provides a general discussion and conclusions.

149 2 Methods

150 2.1 Dynamical cores

151 The atmospheric component of CESM2.2 (Danabasoglu et al., 2020), the Commu-
 152 nity Atmosphere Model, version 6.3 (CAM6; Gettelman et al., 2019; Craig et al., 2021),
 153 supports several different atmospheric dynamical cores. These include dycores on lat-
 154 ion grids, such as finite-volume (FV; Lin, 2004) and Eulerian spectral transform (EUL;
 155 Collins et al., 2006) models, and dycores built on unstructured grids, including spectral-
 156 element (SE; Lauritzen et al., 2018) and finite-volume 3 (FV3; Putman & Lin, 2007) mod-
 157 els. This study compares the performance of the SE and FV dycores, omitting the EUL
 158 and FV3 dycores. CESM2 runs submitted to the Coupled Model Intercomparison Project
 159 Phase 6 (Eyring et al., 2016) used the FV dycore, whereas the SE dycore is often used
 160 for global high-resolution simulations (e.g., Small et al., 2014; Bacmeister & Coauthors,
 161 2018; Chang et al., 2020) due to its higher throughput on massively parallel systems (Dennis
 162 et al., 2012).

163 2.1.1 Finite-volume (FV) dynamical core

164 The FV dycore is a hydrostatic model that integrates the equations of motion us-
 165 ing a finite-volume discretization on a spherical lat-lon grid (Lin & Rood, 1997). The
 166 2D dynamics evolve in floating Lagrangian layers that are periodically mapped to an Eu-

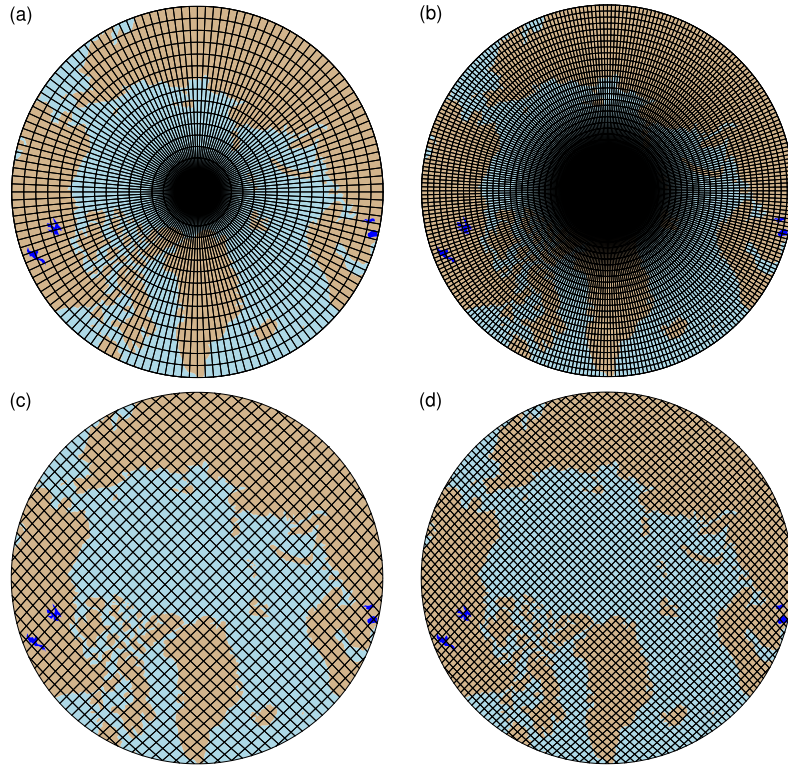


Figure 1. Computational grids for the uniform $1^\circ - 2^\circ$ grids in this study. Grids names after Table 1, (a) f19, (b) f09, (c) ne30pg2 and (d) ne30pg3.

lerian reference grid in the vertical (Lin, 2004). Hyperviscous damping is applied to the divergent modes, and is increased in the top few layers (referred to as a *sponge layer*) to prevent undesirable interactions with the model top, such as wave reflection (Lauritzen et al., 2011). A polar filter damps computational instability due to the convergence of meridians, permitting a longer time step. It takes the form of a Fourier filter in the zonal direction, with the damping coefficients increasing monotonically in the meridional direction (Suarez & Takacs, 1995). The form of the filter is designed to slow down the propagation of large zonal wave-numbers to satisfy the CFL condition of the shortest resolved wave at some reference latitude.

2.1.2 Spectral-element (SE) dynamical core

The SE dycore is a hydrostatic model that integrates the equations of motion using a high-order continuous Galerkin method (Taylor et al., 1997; Taylor & Fournier, 2010). The computational domain is a cubed-sphere grid tiled with quadrilateral elements (see Figure 2). Each element contains a fourth-order basis set in each horizontal direction, with the solution defined at the roots of the basis functions, the Gauss-Lobatto-Legendre quadrature points. This results in 16 nodal points per element, with 12 of the points lying on the (shared) element boundary. Communication between elements uses the direct stiffness summation (Canuto et al., 2007), which applies a numerical flux to the element boundaries to reconcile overlapping nodal values and produce a continuous global basis set.

As with the FV dycore, the dynamics evolve in floating Lagrangian layers that are subsequently mapped to an Eulerian reference grid. A dry mass vertical coordinate was

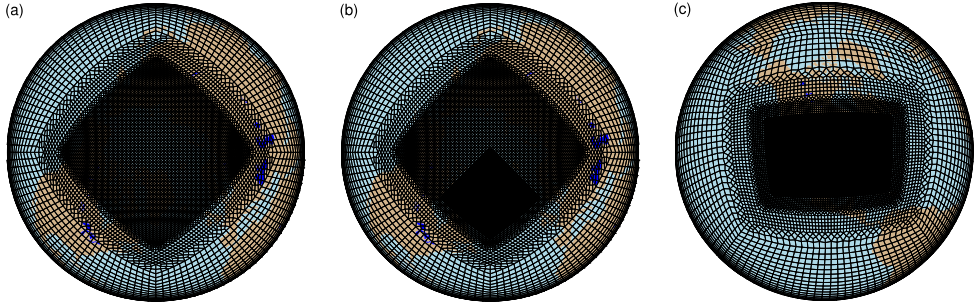


Figure 2. Variable-resolution grids available in CESM2.2, (a) `Arctic`, (b) `Arctic - GrIS` and (c) `CONUS`. Note what is shown is the element grid; the computational grid has 3×3 independent grid points per element.

recently implemented for thermodynamic consistency with condensates (Lauritzen et al., 2018). The 2D dynamics have no implicit dissipation, and so hyperviscosity operators are applied to all prognostic variables to remove spurious numerical errors (Dennis et al., 2012). Laplacian damping is applied in the sponge layer.

The SE dycore supports regional grid refinement via its VR configuration, requiring two enhancements over uniform-resolution setups. Firstly, as the numerical viscosity increases with resolution, explicit hyperviscosity relaxes according to the local element size, reducing in strength by an order of magnitude per halving of the grid spacing. A tensor-hyperviscosity formulation is used (Guba et al., 2014), which adjusts the coefficients in two orthogonal directions to more accurately target highly distorted quadrilateral elements. Secondly, the topography boundary conditions are smoothed in a way that does not excite grid scale modes, and so the NCAR topography software (Lauritzen et al., 2015) has been modified to scale the smoothing radius by the local element size, resulting in rougher topography in the refinement zone.

For SE grids with quasi-uniform grid spacing, the SE tracer transport scheme is replaced with the Conservative Semi-Lagrangian Multi-tracer transport scheme (CSLAM) (Lauritzen et al., 2017). Atmospheric tracers have large, nearly discontinuous horizontal gradients that are difficult to represent with spectral methods, which are prone to oscillatory “Gibbs-ringing” errors (Rasch & Williamson, 1990). CSLAM has improved tracer property preservation and accelerated multi-tracer transport. It uses a separate grid from the spectral-element dynamics, dividing each element into 3×3 control volumes with quasi-equal area. The physical parameterizations are computed from the state on the CSLAM grid, which has clear advantages over the original SE dycore in which the physics are evaluated Gauss-Lobatto-Legendre points (Herrington et al., 2018).

2.2 Grids

We evaluate model simulations on six different grids in this study (Table 1). The FV dycore is run with nominal 1° and 2° grid spacing, referred to as `f09` and `f19`, respectively (Figure 1a,b). We also run the 1° equivalent of the SE-CSLAM grid, referred to as `ne30pg3` (Figure 1d), where ne refers to a grid with $ne \times ne$ elements per cubed-sphere face, and pg denotes that there are $pg \times pg$ control volumes per element for computing the physics. We run an additional 1° SE-CSLAM simulation with the physical parameterizations computed on a grid with 2×2 control volumes per element, `ne30pg2` (Figure 1c; Herrington et al., 2019, note CSLAM is still run on the 3×3 control volume grid).

grid name	dycore	Δx_{eq} (km)	Δx_{refine} (km)	Δt_{phys} (s)
f19	FV	278	-	1800
f09	FV	139	-	1800
ne30pg2	SE-CSLAM	167	-	1800
ne30pg3	SE-CSLAM	111	-	1800
ne30pg3*	SE-CSLAM	111	-	450
Arctic	SE	111	28	450
Arctic – GrIS	SE	111	14	225

Table 1. Grids and dycores used in this study. Δx_{eq} is the average equatorial grid spacing, Δx_{refine} is the grid spacing in the refined region (if applicable), and Δt_{phys} is the physics time step. FV refers to the finite-volume dycore, SE the spectral-element dycore, and SE-CSLAM the spectral-element dycore with CSLAM tracer advection. We use the ne30pg3 grid for two runs with different values of Δt_{phys} .

Three VR meshes were developed for the CESM2.2 release to support grid refinement over the Arctic and the United States (Figure 2). This paper serves as the official documentation of these grids. The VR meshes were developed using the software package SQuadgen (<https://github.com/ClimateGlobalChange/squadgen>). The **Arctic** grid is a 1° grid with $1/4^{\circ}$ regional refinement over the broader Arctic region. The **Arctic–GrIS** grid is identical to the **Arctic** grid, but with an additional patch covering the island of Greenland with $1/8^{\circ}$ resolution. The **CONUS** grid contains $1/8^{\circ}$ refinement over the United States, and 1° everywhere else. The **CONUS** grid is not discussed any further in this paper; see Pfister et al. (2020) for simulations with the **CONUS** grid.

The accuracy of the simulated surface mass balance is expected to be sensitive to grid resolution. Figure 3b shows the average grid spacing over the Greenland Ice Sheet (*GrIS* hereafter) in all six grids in this study. The **ne30pg2** grid has the coarsest representation with an average grid spacing (Δx) of $\Delta x = 160$ km, and the **Arctic–GrIS** grid has the highest resolution with an average grid spacing of $\Delta x = 14.6$ km, similar to the 11 km grid spacing of the RACMO2.3 grid. The **ne30pg3** grid has an average $\Delta x = 111.2$ km, substantially coarser than the **f09** grid, with an average $\Delta x = 60$ km. Although **ne30pg3** and **f09** have similar average grid spacing over the entire globe, and comparable computational costs, the convergence of meridians on the FV grid enhances the resolution over the *GrIS*. The **Arctic** grid has an average grid spacing of $\Delta x = 27.8$ km, and is about 10 times more expensive than the 1° models. The **Arctic–GrIS** grid is about twice as expensive as the **Arctic** grid.

The physics time step depends on the grid resolution. Increased horizontal resolution permits faster vertical velocities that reduce characteristic time scales, so the physics time step is reduced to avoid large time truncation errors (Herrington & Reed, 2018). The **Arctic** and **Arctic–GrIS** grids are run with a $4\times$ and $8\times$ reduction in physics time step relative to the default 1800 s time step used in the 1° and 2° grids (Table 1).

All grids and dycores in this study use 32 hybrid pressure-sigma levels in the vertical, with a model top of 2 hPa or about 40 km. However, note that any grid or dycore can in principle be run with a higher model top or finer vertical resolution.

2.3 Physical parameterizations

All simulations in this study use the CAM6 physical parameterization package (hereafter referred to as the *physics*; Gettelman et al., 2019). The physics in CAM6 differs from its predecessors through the incorporation of high-order turbulence closure, Cloud Layers Unified by Binormals (CLUBB; Golaz et al., 2002; Bogenschutz et al., 2013), which jointly acts as a planetary boundary layer, shallow convection, and cloud macrophysics

scheme. CLUBB is coupled with the MG2 microphysics scheme (Gettelman & Morrison, 2015; Gettelman et al., 2015), which computes prognostic precipitation and uses classical nucleation theory to represent cloud ice for improved cloud-aerosol interactions. Deep convection is parameterized using a convective quasi-equilibrium, mass flux scheme (Zhang & McFarlane, 1995; Neale et al., 2008) and includes convective momentum transport (Richter et al., 2010). Boundary layer form drag is modeled after Beljaars et al. (2004), and orographic gravity wave drag is represented with an anisotropic method informed by the orientation of topographic ridges at the sub-grid scale (the ridge orientation is derived from a high-resolution, global topography dataset (J. J. Danielson & Gesch, 2011)).

Initial simulations with the `ne30pg3` SE grid produced weaker shortwave cloud forcing relative to the tuned finite-volume dycore in the standard CESM2 configuration. The SE dycore in CESM2.2 therefore has two CLUBB parameter changes to provide more realistic cloud forcing and top-of-atmosphere radiation balance. We reduced the width of the sub-grid distribution of vertical velocity (`clubb_gamma` = 0.308 → 0.270) and also reduced the strength of the damping for horizontal component of turbulent energy (`clubb_c14` = 2.2 → 1.6) to increase cloudiness. For a description of how CLUBB parameters impact the simulated climate, see Guo et al. (2015).

2.4 Simulated surface mass balance (SMB)

All grids and dycores simulate the GrIS SMB, which is the sum of mass accumulation of precipitation and mass loss from ablation. The latter is the sum of evaporation, sublimation and liquid runoff, with runoff being a combination of liquid precipitation and snow and ice melt. Not all liquid precipitation or snow/ice melt runs off the ice sheet; this water can penetrate pore spaces in the snowpack/firn layer and freeze, increasing the ice mass. These relevant SMB processes are represented by different CESM components, but it is the Community Land Model, version 5 (CLM; Lawrence et al., 2019), that aggregates these processes and computes the SMB.

CLM runs on the same grid as the atmosphere, and uses a downscaling technique to account for sub-grid variability in SMB. In short, the ice sheet patch in a CLM grid cell is subdivided into 10 elevation classes (ECs), each with a distinct surface energy balance and SMB. The area fraction of each EC is derived from a high-resolution GrIS elevation dataset. The near-surface air temperature, humidity, and air density are calculated for each EC using an assumed lapse rate and the elevation difference from the grid-cell mean. Precipitation from CAM is repartitioned into solid or liquid based on the surface temperature of the EC; precipitation falls as snow for temperatures between $T < -2^{\circ}$ C, as rain for $T > 0^{\circ}$ C, and as a linear combination of rain and snow for temperatures between -2° C and 0° C. Snow accumulation in each EC is limited to a depth of 10 m liquid water equivalent. Any snow above the 10 m cap contributes towards ice accumulation in the SMB. Refreezing of liquid water within the snowpack is an additional source of ice. Integrating over all ECs, weighting by the area fractions, provides a more accurate SMB than would be found using the grid-cell mean elevation. For a more detailed description of how the SMB is computed in CESM, we refer the reader to Lipscomb et al. (2013); Sellevold et al. (2019); van Kampenhout et al. (2020); Muntjewerf et al. (2021).

Changes in ice depth, but not snow depth, count toward the SMB. That is, snow accumulation above the 10 m cap contributes a positive SMB, and surface ice melting (after melting of the overlying snow) yields a negative SMB. Since snow in the accumulation zone must reach the cap to simulate a positive SMB, the snow depths on the VR grids were spun up by forcing CLM in standalone mode, cycling over data from a 20-year Arctic FHISt simulation (a model simulation with prescribed, observed sea-surface conditions) for about 500 years. The uniform-resolution grids are initialized with the SMB

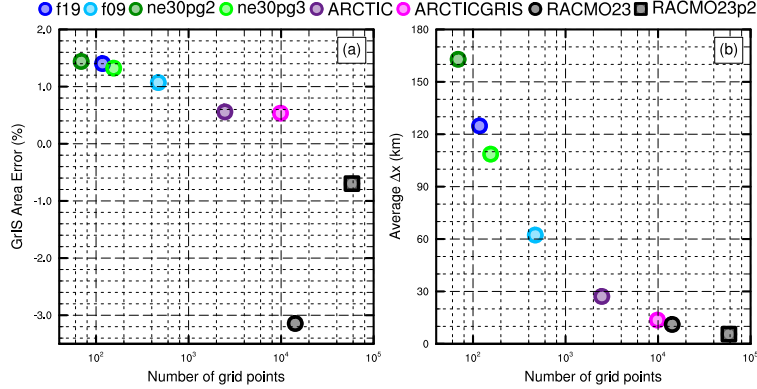


Figure 3. The spatial properties of the GrIS as represented by different grids in this study. (Left) GrIS area error, computed as the relative differences from a 4-km dataset used to create the CESM ice masks, (right) approximate average grid spacing over GrIS.

from an existing **f09** spun-up initial condition. In the simulations described here, the GrIS is prescribed at its observed, modern extent and thickness.

2.5 SMB Analysis

We seek to integrate SMB components over a GrIS ice mask and to diagnose their contributions to the GrIS mass budget. However, the ice masks vary across the grids, especially in comparison to the RACMO3.2 ice mask, whose total area is about 3% less than that of the reference dataset (Figure 3). CLM’s dataset creation tool generates the model ice mask by mapping a high-resolution dataset to the target grid using the Earth System Modeling Framework (ESMF) first-order conservative remapping algorithm (Team et al., 2021). The figure suggests that the mapping errors are less than 1.5% across the CESM2 grids. The area errors in Figure 3 may seem small, but even 1 – 2% area differences can lead to large differences in integrated SMB (Hansen et al., 2022).

We have taken a common-ice-mask approach by mapping all model fields to the lowest-resolution grids, i.e., the **f19** and **ne30pg2** grids, and integrating over these low-resolution ice masks. The use of low-resolution common ice masks is a conservative decision, and is justified because we seek to use first-order remapping algorithms to map fields to the common ice mask, which is not generally reliable when mapping to a higher-resolution grid than the source grid. We use two remapping algorithms: ESMF first-order conservative and the TempestRemap (Ullrich & Taylor, 2015) high-order monotone algorithm. Since mapping errors are sensitive to grid type, we evaluate all quantities on both common ice masks, the **f19** and **ne30pg2** masks. Thus, we evaluate an integrated quantity on a given grid up to four times to estimate the uncertainty due to differences in grid type and remapping algorithms.

The SMB is expressed in a form that is agnostic of water phase, a total water mass balance, to facilitate comparisons across different grids with different ice masks and to increase consistency with the variables available in the RACMO datasets. The SMB for total water can be expressed as:

$$SMB = \text{accumulation} + \text{runoff} + \text{evaporation}/\text{sublimation}, \quad (1)$$

where all terms have consistent sign conventions (positive values contribute mass, and negative values reduce mass). The accumulation source term refers to the combined solid and liquid precipitation, runoff refers to the liquid water sink, and evaporation/sublimation

338 is the vapor sink. Since the runoff term aggregates many processes, we isolate the melting
 339 contribution by also tracking the combined melt of snow and ice. Note that this SMB
 340 expression is different from the internally computed SMB described in the previous sec-
 341 tion.

342 We consider two approaches for mapping and integrating the SMB components over
 343 the common ice masks:

- 344 1. Map the grid-cell mean quantities to the common grid, and integrate the mapped
 345 fields over the common ice masks.
- 346 2. Map the patch-level quantities (i.e., the state over the ice fractional component
 347 of the grid cell) to the common grid, and integrate the mapped fields over the com-
 348 mon ice masks.

349 Note that we are mapping to low-resolution grids that have larger GrIS areas than
 350 the source grids (Figure 3). Since the components of equation 1 are not confined to the
 351 ice mask, method 1 reconstructs the SMB over the portion of the common ice mask that
 352 is outside the ice mask on the source grid. While this may be a an acceptable way to re-
 353 construct the mass source terms over different ice masks, ice melt is zero outside the source
 354 ice mask, and so method 1 will underestimate the mass sink term. This underestima-
 355 tion is systematic in method 2, where all variables are exclusive to the ice mask; map-
 356 ping to a lower-resolution grid will dilute a field of non-zero values over the ice mask with
 357 a field of zeros outside the ice mask. However, patch-level values for processes exclusive
 358 to the ice mask (e.g., ice melt) will on average have larger magnitudes than the the grid-
 359 mean quantities used in method 1.

360 The different error characteristics of the two methods are used to diversify the en-
 361 semble. Each of the four regridding combinations (with conservative and high-order remap-
 362 ping to the f09 and ne30pg2 grids) are repeated with each method, resulting in (up to)
 363 eight values for each integrated quantity. Unfortunately, the patch-level values of evap-
 364 oration/sublimation are not available from the model output, and we estimate their con-
 365 tribution by zeroing out the field for grid cells that have no ice, prior to mapping to the
 366 common ice mask. This will degrade the SMB estimates using method 2, however we
 367 are more interested in characterizing the behavior of individual processes across grids
 368 and dycores, expressed as the components of the SMB, rather than the SMB itself.

369 2.6 Experimental design

370 All simulations described here use an identical transient 1979-1998 Atmospheric
 371 Model Inter-comparison Project (AMIP) configuration, with prescribed monthly sea-surface
 372 temperature and sea ice following Hurrell et al. (2008). In CESM terminology, AMIP
 373 simulations use the FHIST computational set and run out of the box in CESM2.2.

374 2.7 Observational Datasets

375 We use several observational datasets (Table 2) to assess the performance of the
 376 simulations. SMB datasets are gathered from multiple sources. Regional Atmospheric
 377 Climate Model, version 2.3 11km (RACMO23; Noël et al., 2015) and version 2.3p2 5.5km
 378 (RACMO2.3p2; Noël et al., 2018, 2019) are RCM simulations targeting Greenland, forced
 379 by ERA renalyses products at the domain's lateral boundaries. The RACMO simula-
 380 tions have been shown to perform skillfully against observations and are often used as
 381 modeling targets (e.g., Evans et al., 2019; van Kampenhout et al., 2020).

382 In-situ SMB (snow pit and ice cores) and radar accumulation datasets (e.g., Ice-
 383 Bridge) are maintained in The Land Ice Verification and Validation toolkit (LIVVkit),
 384 version 2.1 (Evans et al., 2019). However, these point-wise measurements are difficult

data product	years used in this study	resolution	citation
ERA5	1979-1998	1/4°	Copernicus (2019)
CERES-EBAF ED4.1	2003-2020	1°	Loeb et al. (2018)
CALIPSO-GOCCP	2006-2017	1°	Chepfer et al. (2010)
RACMO2.3	1979-1998	11 km	Noël et al. (2015)
RACMO2.3p2	1979-1998	5.5 km	Noël et al. (2019)

Table 2. Description of observational datasets used in this study.

385 to compare to model output spanning several different grids, especially since the SMB
 386 from each elevation class is not available from the model output. We used a nearest-neighbor
 387 technique for an initial analysis, which showed that the model biases are similar to those
 388 computed using the RACMO datasets. Because of the uncertainty of comparing grid-
 389 ded fields to point-wise measurements, and the lack of information added with regard
 390 to model biases, we omitted these datasets from our analysis.

391 3 Results

392 3.1 Tropospheric temperatures

393 Before delving into the simulated Arctic climate conditions, we assess the global
 394 mean differences between the various grids and dycores. Figure 4 shows 1979-1998 an-
 395 nual mean, zonal mean height plots expressed as differences between uniform-resolution
 396 grids and dycores. The **f09** grid is warmer than the **f19** grid, primarily in the mid-to-
 397 high latitudes throughout the depth of the troposphere. This is a common response to
 398 increasing horizontal resolution in GCMs (Pope & Stratton, 2002; Roeckner et al., 2006).
 399 Herrington and Reed (2020) have shown that this occurs in CAM due to higher resolved
 400 vertical velocities which, in turn, generate more condensational heating in the CLUBB
 401 macrophyiscs. The right panel in Figure 4a supports this interpretation, showing an in-
 402 crease in the climatological CLUBB heating at all latitudes in the **f09** grid, but with the
 403 largest increase in the mid-latitudes.

404 As the SE dycore is less diffusive than the FV dycore, the resolved vertical veloc-
 405 ities are larger in the SE dycore, and so the **ne30pg3** troposphere is modestly warmer
 406 than **f09** (Figure 4b). The stratosphere responds differently, with **ne30pg3** much cooler
 407 than **f09** in the mid-to-high latitudes. Figure 4c also shows small temperature differences
 408 between **ne30pg3** and **ne30pg2**, with **ne30pg3** slightly warmer near the tropopause at
 409 high latitudes. This is consistent with the similar climates found for these two grids by
 410 Herrington et al. (2019).

411 Comparing the VR grids to the uniform-resolution grids is complicated because we
 412 simultaneously increase the resolution and reduce the physics time-step, both of which
 413 influence the solution (Williamson, 2008). We therefore run an additional **ne30pg3** sim-
 414 ulation with the shorter physics time step used in the **Arctic** grid (450 s), referred to
 415 as **ne30pg3*** (Table 1). Figure 5a shows the difference between **ne30pg3*** and **ne30pg3**
 416 for climatological summer temperatures in zonal-mean height space. The troposphere
 417 is warmer with the reduced time step, and the mechanism is similar in that the shorter
 418 time step increases resolved vertical velocities (not shown) and CLUBB heating (right
 419 panel in Figure 5a). Figure 5b shows the difference in climatological summer temper-
 420 ature between the **Arctic** grid and the **ne30pg3*** grid. With the same physics time step,
 421 the greater condensational heating and warmer temperatures are confined to the refined
 422 Arctic region.

423 Figure 5c shows that the **Arctic-GrIS** grid is much warmer than the **Arctic** grid
 424 in the Arctic summer. This may be due, in part, to the shorter physics time step, but

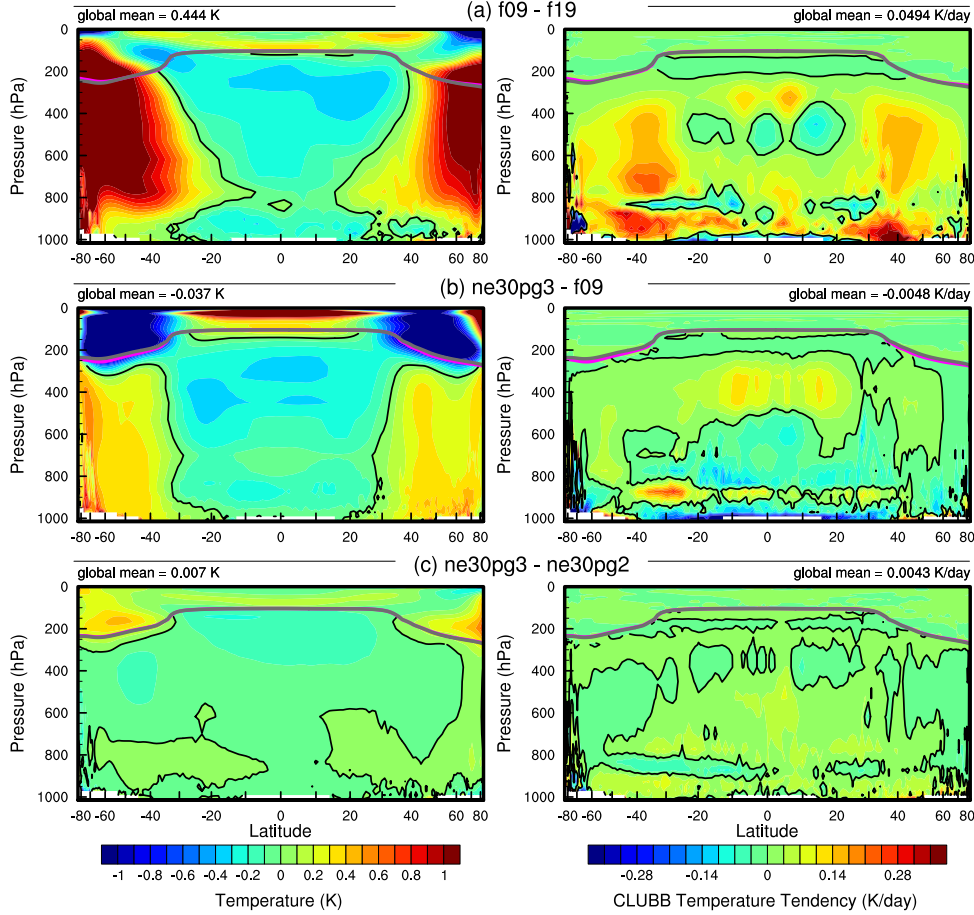


Figure 4. 1979–1998 annual mean temperature (left column) and CLUBB temperature tendencies (right column) in zonal mean height space, expressed as differences between the various 1° – 2° grids. The thick grey and magenta lines are the tropopause for the control run and the test run, respectively.

the temperature response is too large to be explained by enhanced condensational heating from CLUBB alone. This summer warming appears to be a result of variations in the stationary wave pattern, with a swath of anomalous southerly winds to the west of Greenland (not shown). This dynamic response is interesting, because other than the physics time step, the only difference between the Arctic – GrIS and Arctic runs is the doubling of resolution over Greenland. This behavior will be explored further in a future study.

It is useful to understand summer temperature biases due to their control on ice and snow melt over the GrIS (Ohmura, 2001). Figure 6 shows the 1979–1998 lower troposphere summer temperature bias relative to ERA5, computed by equating a layer mean virtual temperature with the 500–1000 hPa geopotential thickness. The results are consistent with the zonal mean height plots; increasing resolution from f19 to f09 warms the climate, and the 1° SE grids are warmer than the FV grids. The FV summer temperatures are persistently colder than ERA5, whereas the 1° SE grids are not as cold, and are actually warmer than ERA5 at high-latitudes, north of 75° . All grids show a north-south gradient in bias over Greenland, with the summer temperature bias more positive

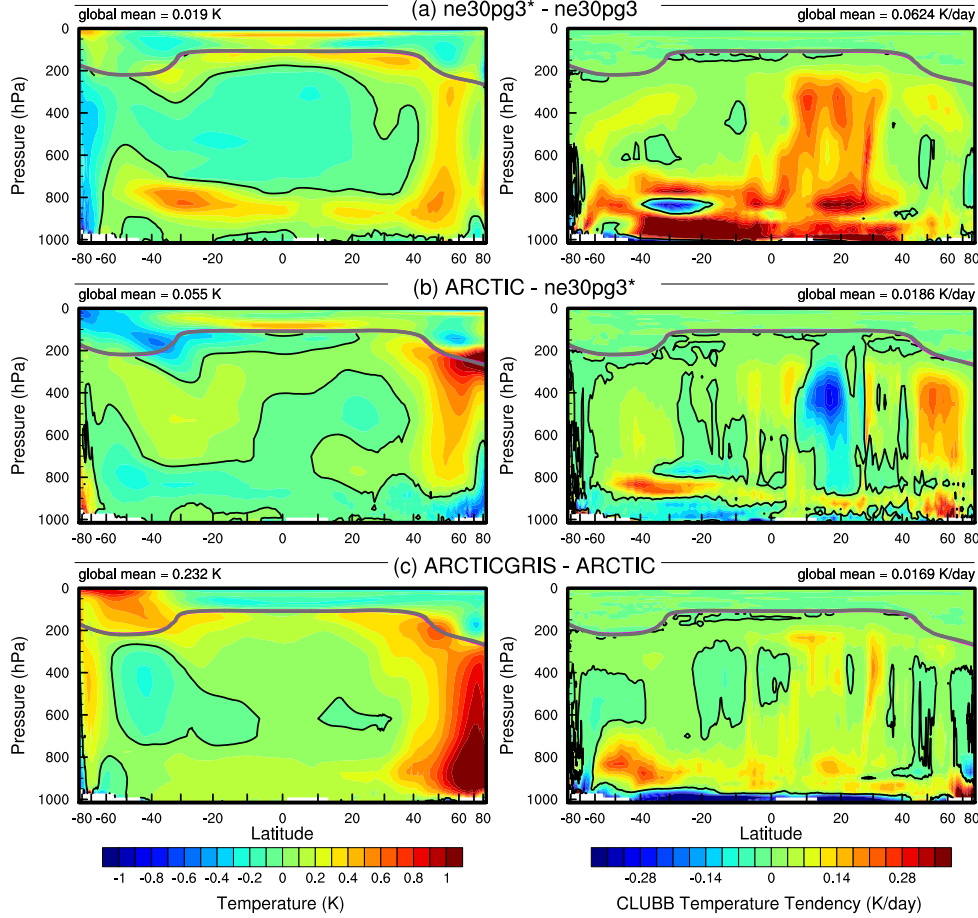


Figure 5. As in Figure 4 but for the short-time-step experiment and the VR grids. The fields plotted are for the climatological northern hemisphere summer. We focus on summer because that is when the resolution response is largest, and the refined regions are located in the northern hemisphere.

for the northern part of the ice sheet. This pattern is also evident in the near surface temperature bias over Greenland (not shown).

The Arctic grid has summer temperatures similar to the 1° SE grids, but is slightly warmer over northern Eurasia and the North Pole (Figure 6). An anomalous cooling patch forms to the west of Greenland, centered over Baffin Island. The Arctic – GrIS grid is warmer than the Arctic grid over most of the Arctic, but with a similar spatial pattern of summer temperature bias.

Some of these temperature differences may be related to differences in summer cloudiness. Figure 7 shows the summer shortwave cloud forcing bias in the six runs, using the CERES product. Shortwave cloud forcing quantifies the impact of clouds on shortwave radiation, taken as the difference between all-sky and clear-sky shortwave radiative fluxes at the top of the atmosphere. A negative bias corresponds to excessive reflection and cooling. The uniform grids have similar biases, with the clouds reflecting 20–40 W/m² too much shortwave radiation over a wide swath of the Arctic, primarily the land masses. There is also a halo of positive bias (clouds not reflective enough) around the ocean perimeter of Greenland. The Arctic grid has much smaller cloud forcing biases over the Arc-

tic land masses, but is still too reflective over Alaska, the Canadian Archipelago, and parts of Eurasia. Compared to the **Arctic** grid, the **Arctic – GrIS** grid vastly reduces the cloud forcing bias over Eurasia, and also improves the bias over North America. In both VR grids, the halo of positive shortwave cloud forcing bias around the perimeter of Greenland is absent.

The summer cloud forcing biases are consistent with the summer temperature biases in Figure 6 – regions where clouds are too reflective coincide with regions that are too cold. While we have not quantified the contribution of cloud biases to the cooler Arctic temperatures, shortwave radiation is a crucial component of the Arctic energy budget during summer. The shortwave cloud forcing biases are on the order of 10 W/m², which is a significant fraction of the total absorbed shortwave during Arctic summer (Serreze et al., 2007) and is therefore likely a factor contributing to the cooler temperatures.

3.2 Clouds and precipitation over Greenland

In addition to summer temperatures, shortwave radiation is an important determinant of snow and ice melt. Figure 8 shows the summer incident shortwave radiation bias at the surface over Greenland and surrounding seas. The top panel shows the bias relative to the RACMO2.3p2 dataset, and the middle panel relative to the CERES dataset. The halo of excessive incident shortwave radiation around the coasts of Greenland is apparent for both datasets in relation to the coarser grids, consistent with the shortwave cloud forcing biases in Figure 7.

The ice sheet interior receives too little shortwave radiation in the coarser grids. On the VR grids, both the interior shortwave deficit and the excessive shortwave around the ocean perimeter are improved. This suggests that the coarse grid clouds are too thick in the interior of Greenland and too thin around the perimeter, which is consistent with the total summer cloud fraction bias, computed from the CALIPSO cloud dataset and shown in the bottom panel of Figure 8. Note that total cloud fraction characterizes the cloud field at all vertical levels, and attenuates the changes arising from any single layer due to the occurrence of overlapping clouds at other levels. The VR grids exhibit an overall improvement in total cloud fraction bias, relative to the coarse grids.

The top panel of Figure 9 show the annual climatological mean precipitation bias over the GrIS, expressed as the fractional difference from the RACMO2.3p2 solution. The coarse 1° – 2° grids have large, positive biases centered over the southern dome. The **Arctic** grid reduces this bias substantially, and the **Arctic–GrIS** grid reduces it further, with precipitation centers migrating from the interior toward the margins.

The more accurate representation of orographic precipitation in the VR grids is consistent with the cloud and radiation biases, cf. Figures 7, 8, and 9. The agreement of the cloud, radiation and precipitation biases in and around Greenland from multiple independent datasets indicates that the biases are a robust feature of the coarser grids. The reduced biases in the VR grids suggest that the deficiencies of the coarse grids are due to insufficient horizontal resolution, consistent with previous findings that coarse GCMs have large, positive precipitation biases over Greenland (Pollard & Groups, 2000; van Kampenhout et al., 2018).

3.3 Greenland surface mass balance

Table 3 shows the 1979-1998 climatological SMB components for each grid, compared with RACMO. The values in the table are averages over the ensemble of mapping methods to the common ice masks described in section 2.5, and the RACMO values are averages over both RACMO datasets (Table 2). Table 3 also contains (in parenthesis) the SMB components derived from evaluating the integrals on each model's native grid and ice mask. Of note is the large reduction in melt rates compared to the values com-

grid name	accumulation	total melt	runoff	sublimation	SMB
RACMO	681.7 (733.5)	-318.6 (-436.4)	-189.1 (-258.5)	-34.5 (-38.8)	458.1 (436.2)
ne30pg2	1007. (973.4)	-519.9 (-647.3)	-381.9 (-347.0)	-33.9 (-32.1)	591.2 (594.3)
ne30pg3	931.0 (909.3)	-540.8 (-686.7)	-375.8 (-330.1)	-34.1 (-32.6)	521.2 (546.6)
f19	884.9 (913.5)	-414.0 (-546.5)	-284.0 (-284.3)	-36.5 (-37.5)	564.4 (591.7)
f09	873.9 (882.1)	-389.1 (-482.3)	-256.1 (-212.3)	-37.3 (-37.4)	580.5 (632.4)
Arctic	784.1 (818.6)	-335.5 (-436.8)	-215.8 (-194.2)	-42.4 (-43.9)	526.0 (580.5)
Arctic – GrIS	693.8 (747.3)	-437.3 (-610.4)	-276.8 (-307.8)	-48.1 (-51.8)	369.0 (387.7)

Table 3. 1979–1998 surface mass balance of the Greenland Ice Sheet in Gt/yr. Values shown are using the common ice mask approach described in the methods section, whereas values in parentheses are from integrating over the native grid and ice mask.

puted on the native grid, illustrating the dissipation of this quantity discussed in section 2.5. For integrated precipitation, the differences between the native and common-ice-mask approaches are much smaller, since the combined solid/liquid precipitation rates are not directly tied to the ice mask.

The coarse grids are characterized by too much precipitation and too much melting and runoff, compared with RACMO. The SMB in coarse grids therefore have smaller errors than their individual components (Table 3), because large errors in the source and sink terms offset one another when added together. Such compensating errors highlights the importance of understanding the extent to which a model is getting the SMB right for the right reasons.

Figure 10 shows time series of annually integrated precipitation and snow/ice melt over the GrIS for the various different grids and dycores, and RACMO in black. The 1979–1998 climatological mean values from Table 3 are shown as circles on the right side of the panels. The uniform $1^\circ - 2^\circ$ grids have positive precipitation biases, whereas the VR grids have the smallest biases, with precipitation comparable to RACMO. The f19 and f09 grids perform similarly, with +110 Gt/yr bias, whereas ne30pg3 is biased by about +165 Gt/yr and ne30pg2 by +230 Gt/yr.

The combined annual snow/ice melt shown in the bottom panel of Figure 10 indicates that the Arctic grid simulates the most realistic melt rates, with the other grids having more melt than RACMO. The Arctic–GrIS grid over-predicts melting by about 125 Gt/yr. This is likely due to an anomalously warm lower troposphere during the summer, relative to the Arctic run (Figure 6). The f19 and f09 melting rates are improved over Arctic–GrIS, overestimating melt by only 70–90 Gt/yr. The SE grids have the largest positive melt bias, between 200–220 Gt/yr.

To illustrate the regional behavior of the SMB components, Figure 11 shows the precipitation and combined snow/ice melt integrated over the basins defined by Rignot and Mouginot (2012). The uncertainty due to differences in basin area is larger than for GrIS-wide integrals, owing to the differences in basin boundaries on the common ice masks, which are shown in the f19 and ne30pg2 panels of Figure 9. Nonetheless, the regional totals in Figure 11 correctly show the southeast and southwest basins have the most accumulation. In all basins, accumulation decreases monotonically with increasing grid resolution, though with some exceptions. The Arctic–GrIS grid simulates less precipitation than RACMO in the central-east and southeast basins, and is closest of all grids to RACMO in the large southwest basin.

The basin-integrated melt rates in Figure 11 depend on the dycore. The uniform-resolution SE grids have the largest positive biases in all basins. The Arctic–GrIS grid is a close second, while the FV grids have systematically smaller melt-rates. The “second-place” standing of Arctic–GrIS is somewhat unexpected, as this grid has the warmest

544 lower-troposphere summer temperatures (Figure 6) and greatest incident shortwave ra-
 545 diation (Figure 8), yet it has less melting than the uniform-resolution SE grids.

546 Lower troposphere temperature is not a strict proxy for melting; e.g., it may not
 547 capture microclimate effects as a result of a better representation of the low-elevation
 548 ablation zones. The Positive Degree-Day temperature based melt index (PDD; Braith-
 549 waite, 1984), which accumulate the near-surface temperature in $^{\circ}\text{C}$ for days with tem-
 550 perature above freezing, is a more accurate proxy for melting. PDD is nonlinear in mean
 551 monthly temperature (Reeh, 1991). We compute PDD from monthly mean 2-meter tem-
 552 perature using the method of Calov and Greve (2005), assuming a fixed monthly mean
 553 standard deviation of 3°C and a degree-day factor of $5 \text{ mm d}^{-1} ^{\circ}\text{C}^{-1}$.

554 Figure 11c shows the basin-integrated PDD melt estimate. In the large southeast
 555 and southwest basins (and all the other western basins), the **ne30pg3** grid has larger PDD-
 556 based melt than the **Arctic–GrIS** grid. The FV grids also have large PDD-based melt
 557 in the southwest basin, relative to **Arctic–GrIS**. The PDD plots indicate that the re-
 558 lationship between temperature and melt is not well approximated by the summer lower-
 559 troposphere temperatures in Figure 6.

560 The bottom panel of Figure 9 presents the biases in the combined ice/snow melt
 561 as map plots. These plots show that the largest melt biases are on the southeast and north-
 562 west coasts, where large coarse-grid cells overlap with the ocean. One possibility is that
 563 these problematic grid cells are situated at lower elevations than the true ice sheet sur-
 564 face, leading to a warm bias and too much melt. Figure 12 shows the representation of
 565 the ice sheet surface along two transects on the different grids, compared to the high-
 566 resolution dataset used to generate CAM topographic boundary conditions (J. Daniel-
 567 son & Gesch, 2011; Lauritzen et al., 2015). The two transects are shown in Figure 9: the
 568 east-west “K-transect” in southwest Greenland and a transect extending from the cen-
 569 tral dome down to the Kangerlussuaq glacier on the southeast coast. The 1° – 2° grids
 570 are noticeably coarse, with only a handful of grid cells populating the transect. The **f09**
 571 grid is a bit of an exception since the grid cells narrow in the zonal direction at high lat-
 572 itudes, and a larger number of grid cells can line the east-west transects. The VR grids
 573 are more skillful at reproducing the steep margins of the ice sheet, capturing the char-
 574 acteristic parabolic shape of the GrIS margin.

575 The transects in Figure 12 show that the ice sheet surface on the coarse grids is
 576 not systematically lower than the true surface in ablation zones. Rather, the smooth-
 577 ing and flattening of the raw topography, necessary to prevent the model from exciting
 578 grid-scale numerical modes, causes the lower-elevation ablation zones to extend beyond
 579 the true ice sheet margin, causing the modeled ablation zones (which must reside within
 580 the ice sheet mask) to be elevated relative to the actual ice surface. The **f19** grid has
 581 both the smoothest topography and the flattest ice sheet since its dynamics are coars-
 582 est, whereas the **f09**, **ne30pg2** and **ne30pg3** grids have similar dynamical resolution and
 583 use identical smoothing. This suggests that coarser models will tend to elevate the ab-
 584 lation zones and thereby depress melt rates, which is the opposite of the melt bias that
 585 occurs in the coarse grid simulations.

586 Figure 12 also shows the ice margin boundary, illustrating that the ablation zone
 587 lies in a narrow horizontal band where the ice sheet rapidly plunges to sea-level. Due to
 588 this abrupt transition, coarse grids will commonly represent the ablation zone with grid
 589 cells containing mixtures of ice-covered and ice-free regions. We hypothesize that coarser
 590 models have larger melt biases because summer melting is confined to these mixed ice/land/ocean
 591 grid cells. CLM deals with land heterogeneity in a complex and sophisticated manner,
 592 but CAM only sees the homogenized state after volume averaging over the sub-grid mix-
 593 ture. Thus, warm ice-free land patches in a grid cell may unduly influence the climate
 594 over the entire grid cell, causing a warm bias over the ice-covered patch.

Figure 13 shows the mean melt bias, relative to both RACMO datasets, conditionally sampled based on grid cell ice fraction in the GrIS region. Errors are computed after mapping the melt rates to the common ice masks using different methods, described in section 2.5. The grid cell ice fractions therefore pertain to ice fractions on the low-resolution common ice masks. Also shown are the ± 1 standard deviation of the biases for each bin. The figure shows that coarser grids can be characterized by a monotonic increase in melt bias as the grid cell ice fraction decreases. The VR grids have the smallest melt biases for small grid cell ice fractions (smaller than 50%), the uniform SE grids and f19 have the largest melt biases and the f09 grid melt biases lie between these two cases. Figure 13 generally supports our hypothesis that the prevalence of mixed-grid cells in the ablation zone of coarse grids is responsible for their large melt bias.

3.4 Precipitation extremes

Synoptic storms are tracked using TempestExtremes atmospheric feature detection software (Ullrich et al., 2021). As the **Arctic** grid contains $1/4^\circ$ refinement north of about 45° latitude, the storm tracker is applied to this region for the **Arctic** and **ne30pg3** runs to identify differences in storm characteristics due to horizontal resolution.

Figure 14 shows monthly PDFs of the precipitation rates associated with storms. The PDFs are constructed by sampling all the precipitation rates within 30° of the storm center, for each point on the storm track and for all storms. The PDFs are evaluated on an identical composite grid for all runs, and so storm statistics are not impacted by differences in output resolution. The **Arctic** run has larger extreme precipitation rates compared to **ne30pg3** in every month, but the increase is greatest in the summer months, which coincides with the most extreme events of the year. This is primarily due to increased resolution and not the reduced physics times-step; the **ne30pg3*** run only marginally increases the extreme precipitation rates compared with **ne30pg3** (Figure 14).

The extreme precipitation rates in the **Arctic** run are closer than **ne30pg3** to the ERA5 reanalysis (Figure 14). It is difficult to know how much the extreme precipitation rates in ERA5 are constrained by data assimilation, or whether these precipitation rates are due to using a similar $1/4^\circ$ model as the **Arctic** grid. However, it is well documented that $1/4^\circ$ models are more skillful at simulating extreme events (Bacmeister et al., 2013; Obrien et al., 2016). A more realistic representation of extreme precipitation events is an additional benefit of the VR grids.

4 Conclusions

Running CESM2.2 in an AMIP-style configuration, we have evaluated six grids from two dynamical cores for their performance over the Arctic and in simulating the GrIS SMB. The $1 - 2^\circ$ finite-volume grids have enhanced resolution over polar regions due to their convergence of meridian lines, although a polar filter is used to prevent spurious atmospheric features from forming in these regions. SE grids comparable to the resolution of the FV grids have an isotropic grid structure where the grid resolution is similar over the entire model domain. We developed two VR grids and introduced them into CESM2.2 as part of this work. Both use the SE dycore; the **Arctic** grid has $1/4^\circ$ refinement over the broader Arctic, whereas the **Arctic – GrIS** grid is identical except for a $1/8^\circ$ patch of refinement over Greenland. A third VR grid, **CONUS**, has also been made available in CESM2.2.

In general, the FV grids have colder summer temperatures over the Arctic compared with the SE grids (including the VR grids). The cloud biases in all the uniform-resolution grids, whether FV or SE, are similar, in general being too cloudy over Arctic land masses. It should be emphasized that our analysis is specific to the Arctic sum-

643 mer because of its relevance to GrIS melt rates; an improved representation of clouds
 644 in the Arctic does not imply improved clouds at lower latitudes.

645 At the regional level, there is a halo of negative cloudiness bias around the ocean
 646 perimeter of Greenland on all $1 - 2^\circ$ grids, but not the VR grids. This negative cloud
 647 bias occurs while there is a positive cloud bias over the ice sheet interior. This anomaly
 648 pattern has been attributed to deficient orographic precipitation in the coarser model
 649 grids. With overly smooth topography on the $1 - 2^\circ$ grids, synoptic systems moving into
 650 Greenland are not sufficiently lifted when encountering the steep ice margins. As a re-
 651 sult, excess precipitation falls in the GrIS interior, instead of being concentrated on the
 652 steep coastal margins as shown by observations (Pollard & Groups, 2000; van Kampen-
 653 hout et al., 2018). This results in a positive precipitation and cloud bias in the ice sheet
 654 interior, and a halo of low cloud bias about the perimeter. The agreement of different
 655 observational data products on this bias lends confidence in the attribution of causes.
 656 The VR grids compare better to the observations and show that orographic precipita-
 657 tion in Greenland is largely resolved when the horizontal resolution is increased sufficiently.

658 We integrated the primary source and sink terms of the SMB equation over the GrIS
 659 for each of the six grids. The uniform $1^\circ - 2^\circ$ grids have large positive accumulation bi-
 660 ases because they fail to resolve orographic precipitation. The uniform SE grids have larger
 661 accumulation biases, suggesting that the FV grids are more skillful for precipitation due
 662 to finer resolution over Greenland, and despite a polar filter. The VR grids have the most
 663 accurate accumulation rates of all the grids. The primary mass sink term of the GrIS,
 664 ice/snow melt, have similar biases; the coarse grids melt too much, although the bias is
 665 worse in uniform SE grids. In general, on coarse grids, errors in the individual SMB terms
 666 are larger than the errors in the SMB itself, due to compensating errors. This observa-
 667 tion serves as a precaution; projecting mass-loss from a glacier or ice sheet cannot be re-
 668 liable if the processes representing the components of the SMB are incorrect from the
 669 start, even as the total SMB has the right magnitude.

670 The **Arctic–GrIS** grid has the warmest summer lower troposphere of all grids,
 671 yet it has less melting than the uniform-resolution SE grids. This suggests that grid res-
 672 olution is somehow contributing to the melt biases in coarse grids, in a way that is not
 673 obvious from the large-scale dynamics. We propose a mechanism: coarse grids represent
 674 ablation zones using grid cells with mixed surface types, ice-covered and ice-free. The
 675 warmer ice-free patches may largely determine the mean state, leading to a warm bias
 676 over the ice-covered patches of the grid cell. This mechanism is supported by analysis
 677 of melt biases binned by grid-cell ice fraction.

678 The **Arctic** grid substantially improves the simulated Arctic climate, including pre-
 679 cipitation extremes and the GrIS SMB, compared to the uniform $1^\circ - 2^\circ$ grids. The **Arctic–**
 680 **GrIS** grid has the most realistic cloud and precipitation fields, but its summer temper-
 681 atures are too warm. The 1° FV model gives a surprisingly realistic SMB, likely due to
 682 the relatively fine resolution of Greenland on lat-lon grids (but perhaps also because it
 683 is the most heavily tuned model configuration in CESM). In particular, a greater num-
 684 ber of grid cells in the ablation zone reduces the influence of mixed ice-covered/ice-free
 685 grid cells that represent ablation poorly on the other uniform-resolution grids.

686 As modeling systems move away from lat-lon grids towards quasi-uniform unstruc-
 687 tured grids, it is worth taking stock of whether this will degrade the simulated polar cli-
 688 mate. We have found that the 1° FV model has clear advantages over the 1° SE model
 689 for simulating the GrIS SMB. That is, the simulated GrIS SMB will be adversely im-
 690 pacted in future CESM versions, after the FV dycore is phased out. This finding will not
 691 interrupt the ongoing transition towards unstructured grids in CESM, which is largely
 692 driven by gains in computational efficiency and grid refinement capabilities. We there-
 693 fore provide the the Arctic refined-meshes to the community by way of CESM2.2, pro-

694 viding users the option to simulate a realistic GrIS SMB, although at a substantial com-
 695 putational premium relative to conventional $1^\circ - 2^\circ$ grids.

696 We are working to develop a configuration of the `Arctic` grid that is fully-coupled
 697 with the CESM ocean and sea ice components and the Community Ice Sheet Model (CISM),
 698 to provide multi-century projections of the state of the GrIS and its contribution to sea-
 699 level rise. We have also developed a visualization of the `Arctic-GrIS` run, now avail-
 700 able on youtube¹, to increase awareness of the capabilities of CESM2.2. Figure 15 shows
 701 a snapshot of this visualization, illustrating mesoscale katabatic winds descending the
 702 southeastern slopes of GrIS. These new grids and configurations will provide new oppor-
 703 tunities for CESM polar science and aims to contribute to an improved understanding
 704 of the polar environment. However, we recognize the potentially prohibitive costs for some
 705 users, and so will continue to explore different grids, parameterizations and workflows
 706 that can provide some of the same benefits of the VR grids, but at a lower cost.

707 **Appendix A Details on spectra-element dynamical core improvements 708 since the CESM2.0 release**

709 Since the CESM2.0 release of the spectral-element dynamical core documented in
 710 Lauritzen et al. (2018) some important algorithmic improvements have been implemented
 711 and released with CESM2.2. These pertain mainly to the flow over orography that, for
 712 the spectral-element dynamical core, can lead to noise aligned with the element bound-
 713 aries (Herrington et al., 2018).

714 **A1 Reference profiles**

715 Significant improvement in removing noise for flow over orography can be achieved
 716 by using reference profiles for temperature and pressure

$$T^{(ref)} = T_0 + T_1 \Pi^{(ref)}, \quad (\text{A1})$$

$$p_s^{(ref)} = p_0 \exp\left(-\frac{\Phi_s}{R^{(d)} T_{ref}}\right), \quad (\text{A2})$$

717 (Simmons & Jiabin, 1991) where g gravity, $T_1 = \Gamma_0 T_{ref} c_p^{(d)} / g \approx 192K$ with standard
 718 lapse rate $\Gamma_0 \equiv 6.5K/km$ and $T_0 \equiv T_{ref} - T_1 \approx 97K$; $T_{ref} = 288K$ ($c_p^{(d)}$ specific heat
 719 of dry air at constant pressure; $R^{(d)}$ gas constant for dry air), and Φ_s surface geopoten-
 720 tial. The reference Exner function is

$$\Pi^{(ref)} = \left(\frac{p^{(ref)}}{p_0}\right)^\kappa \quad (\text{A3})$$

721 where $\kappa = \frac{R^{(d)}}{c_p^{(d)}}$. The reference surface pressure $p_0 = 1000hPa$ and at each model level
 722 the reference pressure $p^{(ref)}$ is computed from $p_s^{(ref)}$ and the standard hybrid coefficients

$$p^{(ref)}(\eta) = A(\eta)p_0 + B(\eta)p_s^{(ref)}, \quad (\text{A4})$$

723 where A and B are the standard hybrid coefficients (using a dry-mass generalized ver-
 724 tical mass coordinate η). These reference profiles are subtracted from the prognostic tem-
 725 perature and pressure-level-thickness states before applying hyperviscosity:

CESM2.0 \rightarrow CESM2.2

$$\nabla_\eta^4 T \rightarrow \nabla_\eta^4 \left(T - T^{(ref)}\right), \quad (\text{A5})$$

$$\nabla_\eta^4 \delta p^{(d)} \rightarrow \nabla_\eta^4 \left(\delta p^{(d)} - \delta p^{(ref)}\right). \quad (\text{A6})$$

¹ https://www.youtube.com/watch?v=YwHgqDu75s8&t=4s&ab_channel=NCARVisLab

This reduces spurious transport of temperature and mass up/down-slope due to the hydromechanical viscosity operator.

728 A2 Rewriting the pressure gradient force (PGF)

729 In the CESM2.0 the following (standard) form of the pressure gradient term was
730 used:

$$\nabla_\eta \Phi + \frac{1}{\rho} \nabla_\eta p, \quad (\text{A7})$$

731 where Φ is geopotential and $\rho = \frac{R^{(d)} T_v}{p}$ is density (for details see Lauritzen et al., 2018).
732 To alleviate noise for flow over orography, we switched to an Exner pressure formulation
733 following Taylor et al. (2020), which uses that (A7) can be written in terms of the Exner
734 pressure

$$\nabla_\eta \Phi + c_p^{(d)} \theta_v \nabla_\eta \Pi, \quad (\text{A8})$$

735 where the Exner pressure is

$$\Pi \equiv \left(\frac{p}{p_0} \right)^\kappa. \quad (\text{A9})$$

736 The derivation showing that (A7) and (A8) are equivalent is shown here:

$$\begin{aligned} c_p^{(d)} \theta_v \nabla_\eta \Pi &= c_p^{(d)} \theta_v \nabla_\eta \left(\frac{p}{p_0} \right)^\kappa, \\ &= c_p^{(d)} \theta_v \kappa \left(\frac{p}{p_0} \right)^{\kappa-1} \nabla_\eta \left(\frac{p}{p_0} \right), \\ &= c_p^{(d)} \theta_v \kappa \Pi \left(\frac{p_0}{p} \right) \nabla_\eta \left(\frac{p}{p_0} \right), \\ &= \frac{c_p^{(d)} \theta_v \kappa \Pi}{p} \nabla_\eta p, \\ &= \frac{R^{(d)} \theta_v \Pi}{p} \nabla_\eta p, \\ &= \frac{R^{(d)} T_v}{p} \nabla_\eta p, \\ &= \frac{1}{\rho} \nabla_\eta p. \end{aligned}$$

737 Using the reference states from (Simmons & Jiabin, 1991),

$$\bar{T} = T_0 + T_1 \Pi, \quad (\text{A10})$$

$$\bar{\theta} = T_0 / \Pi + T_1, \quad (\text{A11})$$

738 we can define a geopotential as a function of Exner pressure

$$\bar{\Phi} = -c_p^{(d)} (T_0 \log \Pi + T_1 \Pi - T_1). \quad (\text{A12})$$

739 This "balanced" geopotential obeys

$$c_p^{(d)} \bar{\theta} \nabla \Pi + \nabla \bar{\Phi} = 0 \quad (\text{A13})$$

740 for any Exner pressure. Subtracting this "reference" profile from the PGF yields

$$\begin{aligned} \nabla_\eta \Phi + c_p^{(d)} \theta_v \nabla_\eta \Pi &= \nabla_\eta (\Phi - \bar{\Phi}) + c_p^{(d)} (\theta_v - \bar{\theta}) \nabla_\eta \Pi, \\ &= \nabla_\eta \Phi + c_p^{(d)} \theta_v \nabla_\eta \Pi + c_p^{(d)} T_0 \left[\nabla_\eta \log \Pi - \frac{1}{\Pi} \nabla_\eta \Pi \right]. \end{aligned} \quad (\text{A14})$$

741 In the continuum, the two formulations (left and right-hand side of (A14)) are identi-
742 cal. But under discretization, the second formulation can have much less truncation er-
743 ror.

744 **A3 Results**

745 One year averages of vertical pressure velocity at 500hPa (`OMEGA500`) have been
 746 found to be a useful quantity to detect spurious up or down-drafts induced by steep orog-
 747 raphy (Figure A1). While the true solution is not known, strong vertical velocities aligned
 748 with element edges that are not found in the CAM-FV reference solution (Figure A1(a))
 749 are likely not physical (spurious). The older CESM2.0 version of SE (Figure A1(d)) us-
 750 ing the "traditional" discretization of the PGF, (A14), exhibits significant spurious noise
 751 patters around steep orography compared to CAM-FV (e.g., around Himalayas and An-
 752 des). This is strongly alleviated by switching to the Exner formulation of the PGF (A8;
 753 Figure A1(c)). By also subtracting reference profiles from pressure-level thickness and
 754 temperature, equations (A5) and (A6) respectively, reduces strong up-down drafts fur-
 755 ther (Figure A1(d)). Switching to the CAM-SE-CSLAM version where physics ten-
 756 dencies are computed on an quasi-equal area physics grid and using the CSLAM transport
 757 scheme, marginal improvements are observed in terms of a smoother vertical velocity field
 758 (Figure A1(e,f)). The configuration shown in Figure A1(d) is used for the simulations
 759 shown in the main text of this paper.

760 It is interesting to note that the noise issues and algorithmic remedies found in the
 761 real-world simulations discussed above, can be investigated by replacing all of physics
 762 with a modified version of the Held-Suarez forcing (Held & Suarez, 1994). The original
 763 formulation of the Held-Suarez idealized test case used a flat Earth ($\Phi_s = 0$) and a dry
 764 atmosphere. By simply adding the surface topography used in 'real-world' simulations
 765 and removing the temperature relaxation in the lower part of domain ($\sigma > 0.7$; see Held
 766 and Suarez (1994) for details), surprisingly realistic vertical velocity fields (in terms of
 767 structure) result (see Figure A2). Since this was a very useful development tool it is shared
 768 in this manuscript.

769 **Acknowledgments**

770 This material is based upon work supported by the National Center for Atmospheric Re-
 771 search (NCAR), which is a major facility sponsored by the NSF under Cooperative Agree-
 772 ment 1852977. Computing and data storage resources, including the Cheyenne super-
 773 computer (doi:10.5065/D6RX99HX), were provided by the Computational and Informa-
 774 tion Systems Laboratory (CISL) at NCAR. A. Herrington thanks Matt Rehme (NCAR/CISL)
 775 for his role in generating the Arctic–GrIS visualization available on youtube (https://www.youtube.com/watch?v=YwHgqDu75s&t=4s&ab_channel=NCARVisLab).

777 The data presented in main part of this manuscript is available at <https://github.com/adamrher/2020-arcticgrids>. The source code and data for the Appendix is avail-
 778 able at <https://github.com/PeterHjortLauritzen/CAM/tree/topo-mods>.

780 **References**

- 781 Bacmeister, J. T., & Coauthors. (2018). Projected changes in tropical cyclone activ-
 782 ity under future warming scenarios using a high-resolution climate model. *Cli-
 783 matic Change*, 146, 547-560. Retrieved from <http://dx.doi.org/10.1007/s10584-016-1750-x> doi: 10.1007/s10584-016-1750-x
- 785 Bacmeister, J. T., Wehner, M. F., Neale, R. B., Gettelman, A., Hannay, C., Lau-
 786 ritzen, P. H., ... Truesdale, J. E. (2013). Exploratory high-resolution climate
 787 simulations using the community atmosphere model (cam). *J. Climate*, 27(9),
 788 3073–3099. doi: 10.1175/JCLI-D-13-00387.1
- 789 Bambach, N. E., Rhoades, A. M., Hatchett, B. J., Jones, A. D., Ullrich, P. A., &
 790 Zarzycki, C. M. (2021). Projecting climate change in south america using
 791 variable-resolution community earth system model: An application to chile.
 792 *International Journal of Climatology*.

- 793 Beljaars, A., Brown, A., & Wood, N. (2004). A new parametrization of turbulent
 794 orographic form drag. *Quart. J. Roy. Meteor. Soc.*, *130*(599), 1327–1347. doi:
 795 10.1256/qj.03.73
- 796 Bogenschutz, P. A., Gettelman, A., Morrison, H., Larson, V. E., Craig, C., & Scha-
 797 nen, D. P. (2013). Higher-order turbulence closure and its impact on climate
 798 simulations in the community atmosphere model. *Journal of Climate*, *26*(23),
 799 9655–9676.
- 800 Box, J. E., Bromwich, D. H., & Bai, L.-S. (2004). Greenland ice sheet surface mass
 801 balance 1991–2000: Application of polar mm5 mesoscale model and in situ
 802 data. *Journal of Geophysical Research: Atmospheres*, *109*(D16).
- 803 Braithwaite, R. J. (1984). Calculation of degree-days for glacier-climate research.
 804 *Zeitschrift für Gletscherkunde und Glazialgeologie*, *20*(1984), 1–8.
- 805 Burakowski, E. A., Tawfik, A., Ouimette, A., Lepine, L., Zarzycki, C., Novick, K.,
 806 ... Bonan, G. (2019). Simulating surface energy fluxes using the variable-
 807 resolution community earth system model (vr-cesm). *Theoretical and Applied
 808 Climatology*, *138*(1), 115–133.
- 809 Calov, R., & Greve, R. (2005). A semi-analytical solution for the positive degree-day
 810 model with stochastic temperature variations. *Journal of Glaciology*, *51*(172),
 811 173–175.
- 812 Canuto, C., Hussaini, M. Y., Quarteroni, A., & Zang, T. (2007). *Spectral methods:
 813 Evolution to complex geometries and applications to fluid dynamics* (1st ed.).
 Springer.
- 814 Chang, P., Zhang, S., Danabasoglu, G., Yeager, S. G., Fu, H., Wang, H., ... oth-
 815 ers (2020). An unprecedented set of high-resolution earth system simulations
 816 for understanding multiscale interactions in climate variability and change.
 817 *Journal of Advances in Modeling Earth Systems*, *12*(12), e2020MS002298.
- 818 Chepfer, H., Bony, S., Winker, D., Cesana, G., Dufresne, J., Minnis, P., ... Zeng, S.
 819 (2010). The gcm-oriented calipso cloud product (calipso-goccp). *Journal of
 820 Geophysical Research: Atmospheres*, *115*(D4).
- 821 Collins, W. D., Rasch, P. J., Boville, B. A., Hack, J. J., McCaa, J. R., Williamson,
 822 D. L., ... Zhang, M. (2006). The formulation and atmospheric simulation
 823 of the community atmosphere model version 3 (cam3). *Journal of Climate*,
 824 *19*(11), 2144–2161.
- 825 Copernicus, C. (2019). Era5 monthly averaged data on pressure levels from
 826 1979 to present. URL: <https://cds.climate.copernicus.eu>. doi: 10.24381/
 827 cds.6860a573
- 828 Craig, C., Bacmeister, J., Callaghan, P., Eaton, B., Gettelman, A., Goldhaber, S. N.,
 829 ... Vitt, F. M. (2021). *Cam6.3 user's guide* (Tech. Rep.). NCAR/TN-
 830 571+EDD. doi: 10.5065/Z953-ZC95
- 831 Danabasoglu, G., Lamarque, J.-F., Bacmeister, J., Bailey, D., DuVivier, A., Ed-
 832 wards, J., ... others (2020). The community earth system model ver-
 833 sion 2 (cesm2). *Journal of Advances in Modeling Earth Systems*, *12*(2),
 834 e2019MS001916.
- 835 Danielson, J., & Gesch, D. (2011). *Global multi-resolution terrain elevation data
 836 2010 (GMTED2010)* (Open-File Report 2011-1073). U.S. Geological Survey.
 837 (<http://pubs.usgs.gov/of/2011/1073/pdf/of2011-1073.pdf>)
- 838 Danielson, J. J., & Gesch, D. B. (2011). *Global multi-resolution terrain elevation
 839 data 2010 (GMTED2010)* (Open File Rep. No. 2011-1073). US Geological Sur-
 840 vey. doi: <https://doi.org/10.3133/ofr20111073>
- 841 Dennis, J. M., Edwards, J., Evans, K. J., Guba, O., Lauritzen, P. H., Mirin, A. A.,
 842 ... Worley, P. H. (2012). CAM-SE: A scalable spectral element dynamical
 843 core for the Community Atmosphere Model. *Int. J. High. Perform. C.*, *26*(1),
 844 74–89. Retrieved from <http://hpc.sagepub.com/content/26/1/74.abstract>
 845 doi: 10.1177/1094342011428142
- 846 Evans, K. J., Kennedy, J. H., Lu, D., Forrester, M. M., Price, S., Fyke, J., ... oth-

- 848 ers (2019). Livvkit 2.1: automated and extensible ice sheet model validation.
 849 *Geoscientific Model Development*, 12(3), 1067–1086.
- 850 Eyring, V., Bony, S., Meehl, G. A., Senior, C. A., Stevens, B., Stouffer, R. J., &
 851 Taylor, K. E. (2016). Overview of the coupled model intercomparison project
 852 phase 6 (cmip6) experimental design and organization. *Geoscientific Model
 853 Development*, 9(5), 1937–1958.
- 854 Fettweis, X., Franco, B., Tedesco, M., Van Angelen, J., Lenaerts, J. T., van den
 855 Broeke, M. R., & Gallée, H. (2013). Estimating the greenland ice sheet
 856 surface mass balance contribution to future sea level rise using the regional
 857 atmospheric climate model mar. *The Cryosphere*, 7(2), 469–489.
- 858 Gettelman, A., Callaghan, P., Larson, V., Zarzycki, C., Bacmeister, J., Lauritzen, P.,
 859 ... Neale, R. (2017). Regional climate simulations with the community earth
 860 system model. *J. Adv. Model. Earth Syst.*. (submitted)
- 861 Gettelman, A., Hannay, C., Bacmeister, J. T., Neale, R. B., Pendergrass, A., Dan-
 862 abasoglu, G., ... others (2019). High climate sensitivity in the community
 863 earth system model version 2 (cesm2). *Geophysical Research Letters*, 46(14),
 864 8329–8337.
- 865 Gettelman, A., & Morrison, H. (2015). Advanced two-moment bulk microphysics for
 866 global models. part i: Off-line tests and comparison with other schemes. *Jour-
 867 nal of Climate*, 28(3), 1268–1287.
- 868 Gettelman, A., Morrison, H., Santos, S., Bogenschutz, P., & Caldwell, P. (2015).
 869 Advanced two-moment bulk microphysics for global models. part ii: Global
 870 model solutions and aerosol–cloud interactions. *Journal of Climate*, 28(3),
 871 1288–1307.
- 872 Golaz, J.-C., Larson, V. E., & Cotton, W. R. (2002). A pdf-based model for bound-
 873 ary layer clouds. part i: Method and model description. *Journal of the Atmo-
 874 spheric Sciences*, 59(24), 3540–3551. doi: 10.1175/1520-0469(2002)059<3540:
 875 apbmfb>2.0.co;2
- 876 Guba, O., Taylor, M. A., Ullrich, P. A., Overfelt, J. R., & Levy, M. N. (2014). The
 877 spectral element method (sem) on variable-resolution grids: evaluating grid
 878 sensitivity and resolution-aware numerical viscosity. *Geosci. Model Dev.*, 7(6),
 879 2803–2816. doi: 10.5194/gmd-7-2803-2014
- 880 Guo, Z., Wang, M., Qian, Y., Larson, V. E., Ghan, S., Ovchinnikov, M., ... Zhou,
 881 T. (2015). Parametric behaviors of clubb in simulations of low clouds in the c
 882 ommunity atmosphere model (cam). *Journal of Advances in Modeling Earth
 883 Systems*, 7(3), 1005–1025.
- 884 Hansen, N., Simonsen, S. B., Boberg, F., Kittel, C., Orr, A., Souverijns, N., ... Mot-
 885 tram, R. (2022). Brief communication: Impact of common ice mask in surface
 886 mass balance estimates over the antarctic ice sheet. *The Cryosphere*, 16(2),
 887 711–718.
- 888 Held, I. M., & Suarez, M. J. (1994). A proposal for the intercomparison of the dy-
 889 namical cores of atmospheric general circulation models. *Bull. Am. Meteorol.
 890 Soc.*, 73, 1825–1830.
- 891 Herrington, A. R., Lauritzen, P., Taylor, M. A., Goldhaber, S., Eaton, B. E.,
 892 Bacmeister, J., ... Ullrich, P. (2018). Physics-dynamics coupling with element-
 893 based high-order galerkin methods: quasi equal-area physics grid. *Mon. Wea.
 894 Rev.*, 47, 69–84. doi: 10.1175/MWR-D-18-0136.1
- 895 Herrington, A. R., Lauritzen, P. H., Reed, K. A., Goldhaber, S., & Eaton, B. E.
 896 (2019). Exploring a lower resolution physics grid in cam-se-cslam. *Journal of
 897 Advances in Modeling Earth Systems*, 11.
- 898 Herrington, A. R., & Reed, K. A. (2018). An idealized test of the response of the
 899 community atmosphere model to near-grid-scale forcing across hydrostatic
 900 resolutions. *J. Adv. Model. Earth Syst.*, 10(2), 560–575.
- 901 Herrington, A. R., & Reed, K. A. (2020). On resolution sensitivity in the commu-
 902 nity atmosphere model. *Quarterly Journal of the Royal Meteorological Society*,

- 903 146(733), 3789–3807.
- 904 Hurrell, J. W., Hack, J. J., Shea, D., Caron, J. M., & Rosinski, J. (2008). A new
 905 sea surface temperature and sea ice boundary dataset for the community at-
 906 mosphere model. *Journal of Climate*, 21(19), 5145–5153.
- 907 Jablonowski, C., & Williamson, D. L. (2011). The pros and cons of diffusion, fil-
 908 ters and fixers in atmospheric general circulation models. In P. H. Lauritzen,
 909 C. Jablonowski, M. Taylor, & R. Nair (Eds.), *Numerical techniques for global*
 910 *atmospheric models* (pp. 381–493). Berlin, Heidelberg: Springer Berlin Heidel-
 911 berg. doi: 10.1007/978-3-642-11640-7_13
- 912 Lauritzen, P. H., Bacmeister, J. T., Callaghan, P. F., & Taylor, M. A. (2015). Ncar
 913 global model topography generation software for unstructured grids. *Geosci-
 914 entific Model Development Discussions*, 8(6), 4623–4651. doi: 10.5194/gmdd-8
 915 -4623-2015
- 916 Lauritzen, P. H., Jablonowski, C., Taylor, M., & Nair, R. D. (2010). Rotated
 917 versions of the jablonowski steady-state and baroclinic wave test cases: A
 918 dynamical core intercomparison. *J. Adv. Model. Earth Syst.*, 2(15), 34 pp.
- 919 Lauritzen, P. H., Mirin, A., Truesdale, J., Raeder, K., Anderson, J., Bacmeister, J.,
 920 & Neale, R. B. (2011). Implementation of new diffusion/filtering operators
 921 in the CAM-FV dynamical core. *Int. J. High Perform. Comput. Appl.*. doi:
 922 10.1177/1094342011410088
- 923 Lauritzen, P. H., Nair, R., Herrington, A., Callaghan, P., Goldhaber, S., Dennis, J.,
 924 ... Dubos, T. (2018). NCAR release of CAM-SE in CESM2.0: A reformula-
 925 tion of the spectral-element dynamical core in dry-mass vertical coordinates
 926 with comprehensive treatment of condensates and energy. *J. Adv. Model.*
 927 *Earth Syst.*, 10(7), 1537-1570. doi: 10.1029/2017MS001257
- 928 Lauritzen, P. H., Taylor, M. A., Overfelt, J., Ullrich, P. A., Nair, R. D., Goldhaber,
 929 S., & Kelly, R. (2017). CAM-SE-CSLAM: Consistent coupling of a conser-
 930 vative semi-lagrangian finite-volume method with spectral element dynamics.
 931 *Mon. Wea. Rev.*, 145(3), 833-855. doi: 10.1175/MWR-D-16-0258.1
- 932 Lawrence, D. M., Fisher, R. A., Koven, C. D., Oleson, K. W., Swenson, S. C., Bo-
 933 nan, G., ... others (2019). The community land model version 5: Description
 934 of new features, benchmarking, and impact of forcing uncertainty. *Journal of*
 935 *Advances in Modeling Earth Systems*, 11(12), 4245–4287.
- 936 Lin, S.-J. (2004). A 'vertically Lagrangian' finite-volume dynamical core for global
 937 models. *Mon. Wea. Rev.*, 132, 2293-2307.
- 938 Lin, S.-J., & Rood, R. B. (1997). An explicit flux-form semi-Lagrangian shallow-
 939 water model on the sphere. *Q.J.R.Meteorol.Soc.*, 123, 2477-2498.
- 940 Lipscomb, W. H., Fyke, J. G., Vizcaíno, M., Sacks, W. J., Wolfe, J., Vertenstein,
 941 M., ... Lawrence, D. M. (2013). Implementation and initial evaluation of the
 942 glimmer community ice sheet model in the community earth system model.
 943 *Journal of Climate*, 26(19), 7352–7371.
- 944 Loeb, N. G., Doelling, D. R., Wang, H., Su, W., Nguyen, C., Corbett, J. G., ...
 945 Kato, S. (2018). Clouds and the earth's radiant energy system (ceres) energy
 946 balanced and filled (ebaf) top-of-atmosphere (toa) edition-4.0 data product.
 947 *Journal of Climate*, 31(2), 895–918.
- 948 Lofverstrom, M., Fyke, J. G., Thayer-Calder, K., Muntjewerf, L., Vizcaino, M.,
 949 Sacks, W. J., ... Bradley, S. L. (2020). An efficient ice sheet/earth sys-
 950 tem model spin-up procedure for cesm2-cism2: Description, evaluation, and
 951 broader applicability. *Journal of Advances in Modeling Earth Systems*, 12(8),
 952 e2019MS001984.
- 953 Mottram, R., Boberg, F., Langen, P., Yang, S., Rodehacke, C., Christensen, J. H.,
 954 & Madsen, M. S. (2017). Surface mass balance of the greenland ice sheet in
 955 the regional climate model hirham5: Present state and future prospects. *Low*
 956 *Temp. Sci.*, 75, 105–115.
- 957 Muntjewerf, L., Sacks, W. J., Lofverstrom, M., Fyke, J., Lipscomb, W. H., Er-

- nani da Silva, C., ... Sellevold, R. (2021). Description and Demonstration of the Coupled Community Earth System Model v2–Community Ice Sheet Model v2 (CESM2-CISM2). *Journal of Advances in Modeling Earth Systems*, 13(6), e2020MS002356.
- Neale, R. B., Richter, J. H., & Jochum, M. (2008). The impact of convection on ENSO: From a delayed oscillator to a series of events. *J. Climate*, 21, 5904-5924.
- Noël, B., Van De Berg, W., Van Meijgaard, E., Kuipers Munneke, P., Van De Wal, R., & Van Den Broeke, M. (2015). Evaluation of the updated regional climate model racmo2. 3: summer snowfall impact on the greenland ice sheet. *The Cryosphere*, 9(5), 1831–1844.
- Noël, B., van de Berg, W. J., Lhermitte, S., & van den Broeke, M. R. (2019). Rapid ablation zone expansion amplifies north greenland mass loss. *Science advances*, 5(9), eaaw0123.
- Noël, B., van de Berg, W. J., Van Wessem, J. M., Van Meijgaard, E., Van As, D., Lenaerts, J., ... others (2018). Modelling the climate and surface mass balance of polar ice sheets using racmo2–part 1: Greenland (1958–2016). *The Cryosphere*, 12(3), 811–831.
- Obrien, T. A., Collins, W. D., Kashinath, K., Rübel, O., Byna, S., Gu, J., ... Ullrich, P. A. (2016). Resolution dependence of precipitation statistical fidelity in hindcast simulations. *J. Adv. Model. Earth Syst.*, 8(2), 976–990. Retrieved from <http://dx.doi.org/10.1002/2016ms000671> doi: 10.1002/2016ms000671
- Ohmura, A. (2001). Physical basis for the temperature-based melt-index method. *Journal of applied Meteorology*, 40(4), 753–761.
- Pfister, G. G., Eastham, S. D., Arellano, A. F., Aumont, B., Barsanti, K. C., Barth, M. C., ... others (2020). The multi-scale infrastructure for chemistry and aerosols (musica). *Bulletin of the American Meteorological Society*, 101(10), E1743–E1760.
- Pollard, D. (2010). A retrospective look at coupled ice sheet–climate modeling. *Climatic Change*, 100(1), 173–194.
- Pollard, D., & Groups, P. P. (2000). Comparisons of ice-sheet surface mass budgets from paleoclimate modeling intercomparison project (pmip) simulations. *Global and Planetary Change*, 24(2), 79–106.
- Pope, V., & Stratton, R. (2002). The processes governing horizontal resolution sensitivity in a climate model. *Climate Dynamics*, 19(3-4), 211–236.
- Putman, W. M., & Lin, S.-J. (2007). Finite-volume transport on various cubed-sphere grids. *J. Comput. Phys.*, 227(1), 55–78.
- Rae, J., Adalgeirsdóttir, G., Edwards, T. L., Fettweis, X., Gregory, J., Hewitt, H., ... others (2012). Greenland ice sheet surface mass balance: evaluating simulations and making projections with regional climate models. *The Cryosphere*, 6(6), 1275–1294.
- Rasch, P. J., & Williamson, D. L. (1990). Computational aspects of moisture transport in global models of the atmosphere. *Q. J. R. Meteorol. Soc.*, 116, 1071–1090.
- Reeh, N. (1991). Parameterization of melt rate and surface temperature in the greenland ice sheet. *Polarforschung*, 59(3), 113–128.
- Rhoades, A. M., Huang, X., Ullrich, P. A., & Zarzycki, C. M. (2016). Characterizing sierra nevada snowpack using variable-resolution cesm. *Journal of Applied Meteorology and Climatology*, 55(1), 173–196. Retrieved from <https://doi.org/10.1175/JAMC-D-15-0156.1> doi: 10.1175/JAMC-D-15-0156.1
- Richter, J. H., Sassi, F., & Garcia, R. R. (2010). Toward a physically based gravity wave source parameterization in a general circulation model. *J. Atmos. Sci.*, 67, 136–156. doi: dx.doi.org/10.1175/2009JAS3112.1
- Rignot, E., & Mouginot, J. (2012). Ice flow in greenland for the international polar

- 1013 year 2008–2009. *Geophysical Research Letters*, 39(11).
- 1014 Roeckner, E., Brokopf, R., Esch, M., Giorgetta, M., Hagemann, S., Kornblueh, L.,
 1015 ... Schulzweida, U. (2006). Sensitivity of simulated climate to horizontal
 1016 and vertical resolution in the echam5 atmosphere model. *Journal of Climate*,
 1017 19(16), 3771–3791.
- 1018 Sellevold, R., Van Kampenhout, L., Lenaerts, J., Noël, B., Lipscomb, W. H., &
 1019 Vizcaino, M. (2019). Surface mass balance downscaling through elevation
 1020 classes in an earth system model: Application to the greenland ice sheet. *The
 1021 Cryosphere*, 13(12), 3193–3208.
- 1022 Serreze, M. C., Barrett, A. P., Slater, A. G., Steele, M., Zhang, J., & Trenberth,
 1023 K. E. (2007). The large-scale energy budget of the arctic. *Journal of Geophysical
 1024 Research: Atmospheres*, 112(D11).
- 1025 Simmons, A. J., & Jiabin, C. (1991). The calculation of geopotential and
 1026 the pressure gradient in the ECMWF atmospheric model: Influence on
 1027 the simulation of the polar atmosphere and on temperature analyses.
 1028 *Quart. J. Roy. Meteor. Soc.*, 117(497), 29–58. Retrieved from <https://rmetsonlinelibrary.wiley.com/doi/abs/10.1002/qj.49711749703> doi:
 1029 <https://doi.org/10.1002/qj.49711749703>
- 1030 Small, R. J., Bacmeister, J., Bailey, D., Baker, A., Bishop, S., Bryan, F., ... Verten-
 1031 stein, M. (2014). A new synoptic scale resolving global climate simulation
 1032 using the community earth system model. *J. Adv. Model. Earth Syst.*, 6(4),
 1033 1065–1094. doi: 10.1002/2014MS000363
- 1034 Suarez, M. J., & Takacs, L. L. (1995). Volume 5 documentation of the aries/geos dy-
 1035 namical core: Version 2.
- 1036 Taylor, M. A., & Fournier, A. (2010). A compatible and conservative spectral el-
 1037 ement method on unstructured grids. *J. Comput. Phys.*, 229(17), 5879 - 5895.
 1038 doi: 10.1016/j.jcp.2010.04.008
- 1039 Taylor, M. A., Guba, O., Steyer, A., Ullrich, P. A., Hall, D. M., & Eldred, C.
 1040 (2020). An energy consistent discretization of the nonhydrostatic equations
 1041 in primitive variables. *Journal of Advances in Modeling Earth Systems*, 12(1).
 1042 doi: 10.1029/2019MS001783
- 1043 Taylor, M. A., Tribbia, J., & Iskandarani, M. (1997). The spectral element method
 1044 for the shallow water equations on the sphere. *J. Comput. Phys.*, 130, 92–108.
- 1045 Team, E. J. S., Balaji, V., Boville, B., Collins, N., Craig, T., Cruz, C., ... others
 1046 (2021). *Esmf user guide* (Tech. Rep.).
- 1047 Ullrich, P. A., & Taylor, M. A. (2015). Arbitrary-order conservative and consis-
 1048 tent remapping and a theory of linear maps: Part i. *Monthly Weather Review*,
 1049 143(6), 2419–2440.
- 1050 Ullrich, P. A., Zarzycki, C. M., McClenney, E. E., Pinheiro, M. C., Stansfield, A. M.,
 1051 & Reed, K. A. (2021). Tempestextremes v2. 1: a community framework for
 1052 feature detection, tracking and analysis in large datasets. *Geoscientific Model
 1053 Development Discussions*, 1–37.
- 1054 Van Angelen, J., Lenaerts, J., Lhermitte, S., Fettweis, X., Kuipers Munneke, P.,
 1055 Van den Broeke, M., ... Smeets, C. (2012). Sensitivity of greenland ice
 1056 sheet surface mass balance to surface albedo parameterization: a study with a
 1057 regional climate model. *The Cryosphere*, 6(5), 1175–1186.
- 1058 van Kampenhout, L., Lenaerts, J. T., Lipscomb, W. H., Lhermitte, S., Noël, B.,
 1059 Vizcaíno, M., ... van den Broeke, M. R. (2020). Present-day greenland ice
 1060 sheet climate and surface mass balance in cesm2. *Journal of Geophysical
 1061 Research: Earth Surface*, 125(2).
- 1062 van Kampenhout, L., Rhoades, A. M., Herrington, A. R., Zarzycki, C. M., Lenaerts,
 1063 J. T. M., Sacks, W. J., & van den Broeke, M. R. (2018). Regional grid refine-
 1064 ment in an earth system model: Impacts on the simulated greenland surface
 1065 mass balance. *The Cryosphere Discuss.*. doi: 10.5194/tc-2018-257
- 1066 Wan, H., Giorgetta, M. A., Zängl, G., Restelli, M., Majewski, D., Bonaventura, L.,

- 1068 ... others (2013). "the icon-1.2 hydrostatic atmospheric dynamical core on
1069 triangular grids, part i: formulation and performance of the baseline version".
1070 *Geosci. Model Dev.*, 6, 735–763.
- 1071 Williamson, D. (2007). The evolution of dynamical cores for global atmospheric
1072 models. *J. Meteor. Soc. Japan*, 85, 241-269.
- 1073 Williamson, D. (2008). Convergence of aqua-planet simulations with increasing res-
1074 olution in the community atmospheric model, version 3. *Tellus A*, 60(5), 848–
1075 862. doi: 10.1111/j.1600-0870.2008.00339.x
- 1076 Zarzycki, C. M., Jablonowski, C., & Taylor, M. A. (2014). Using variable-resolution
1077 meshes to model tropical cyclones in the community atmosphere model. *Mon.
1078 Wea. Rev.*, 142(3), 1221-1239. doi: 10.1175/MWR-D-13-00179.1
- 1079 Zhang, G., & McFarlane, N. (1995). Sensitivity of climate simulations to the
1080 parameterization of cumulus convection in the canadian climate center general-
1081 circulation model. *ATMOSPHERE-OCEAN*, 33(3), 407-446.

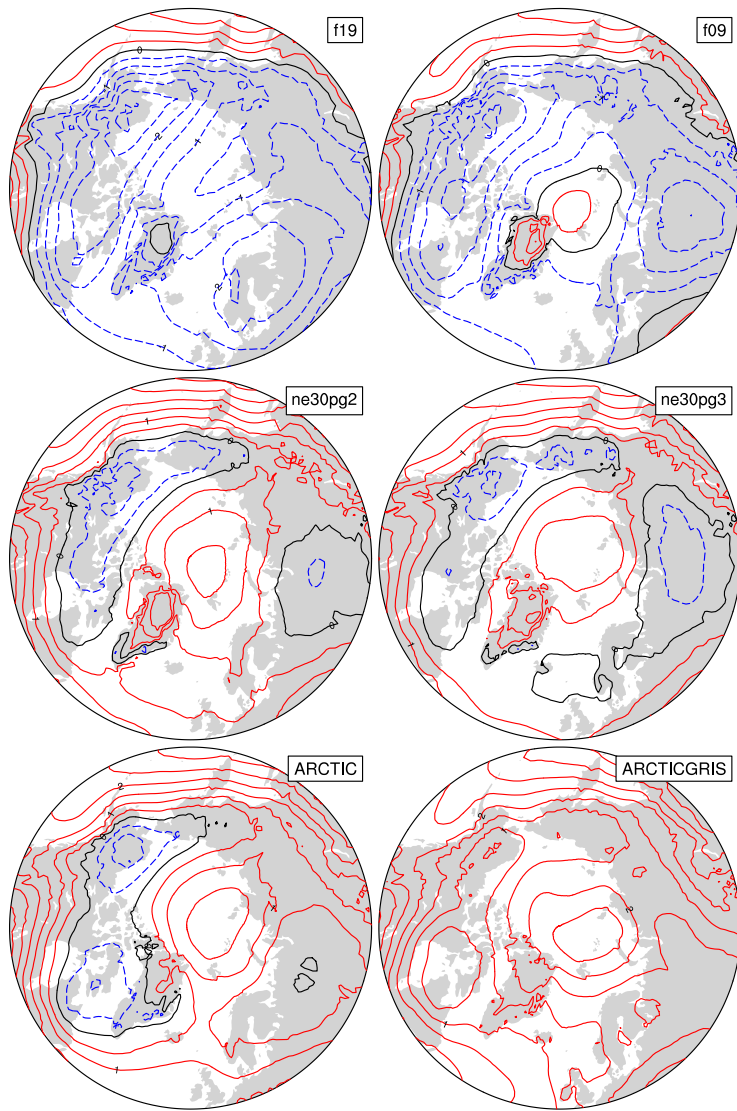


Figure 6. 1979-1998 lower troposphere, northern hemisphere summer virtual temperature biases, computed as the difference from ERA5. Lower troposphere layer mean virtual temperature is derived from the 1000 hPa - 500h Pa geopotential thickness, using the hypsometric equation. Differences are computed after mapping the ERA5 data to the finite-volume grids since the geopotential field is only available on the output tapes in the spectral-element runs that have been interpolated to the f09 grid, inline.

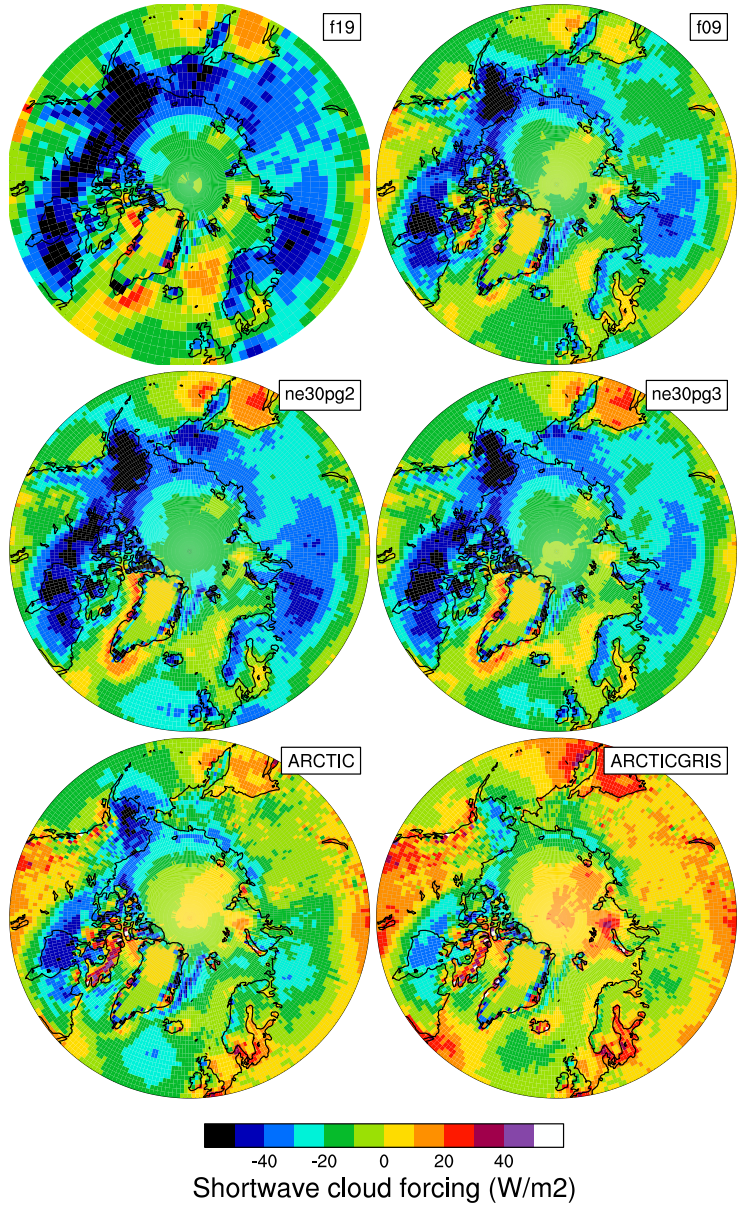


Figure 7. 1979-1998 Northern Hemisphere summer shortwave cloud forcing bias, relative to the CERES-EBAF gridded dataset. Shortwave cloud forcing is defined as the difference between all-sky and clear-sky net shortwave fluxes at the top of the atmosphere. Differences are computed after mapping all model output to the 1° CERES-EBAF grid.

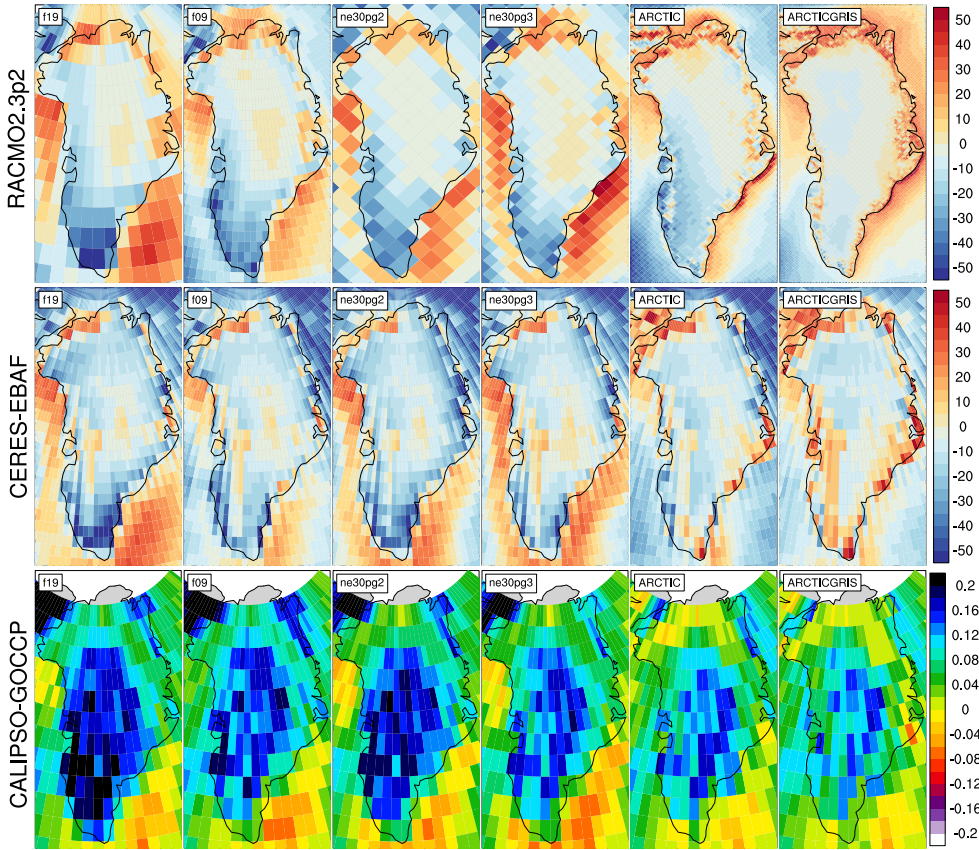


Figure 8. 1979-1998 northern hemisphere summer (top) total cloud fraction bias relative to the CALIPSO dataset and incident shortwave radiation bias (W/m^2), computed as the difference (middle) from CERES, and (bottom) RACMO2.3p2 dataset. The CALIPSO and CERES differences are found by mapping the model output to the 1° grid, and differences in the bottom panel are computed after mapping the RACMO2.3p2 dataset to the individual model grids. Note that the averaging period for the CALIPSO-GOCCP and CERES-EBAF panels, 2006-2017 and 2003-2020, respectively, are different from the averaging period for the model results.

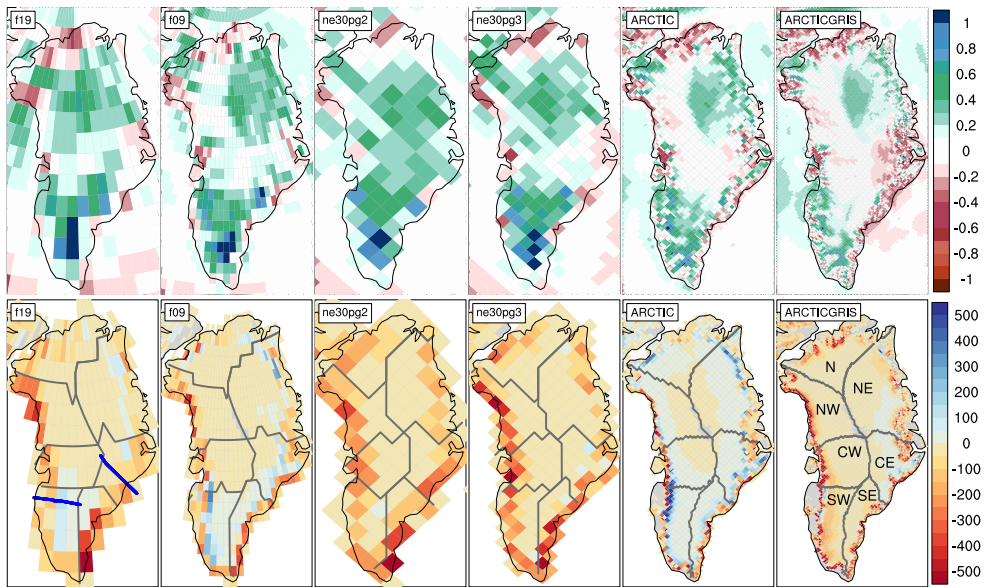


Figure 9. 1979-1998 (top) annual precipitation and (bottom) ice/snow melt biases relative to RACMO2.3p2, evaluated on the native model grids. The precipitation biases are expressed as fractional changes, whereas the melt biases are absolute changes (mm/yr). In the bottom panel, the Rignot and Mouginot (2012) basin boundaries are shown in grey for each model grid. Note that Figure 11 uses the basin boundaries for the two common ice masks, shown in the f19 and ne30pg2 panels, in computing the basin-scale integrals. Blue lines in the f19 panel show the location of the two transects plotted in Figure 12..

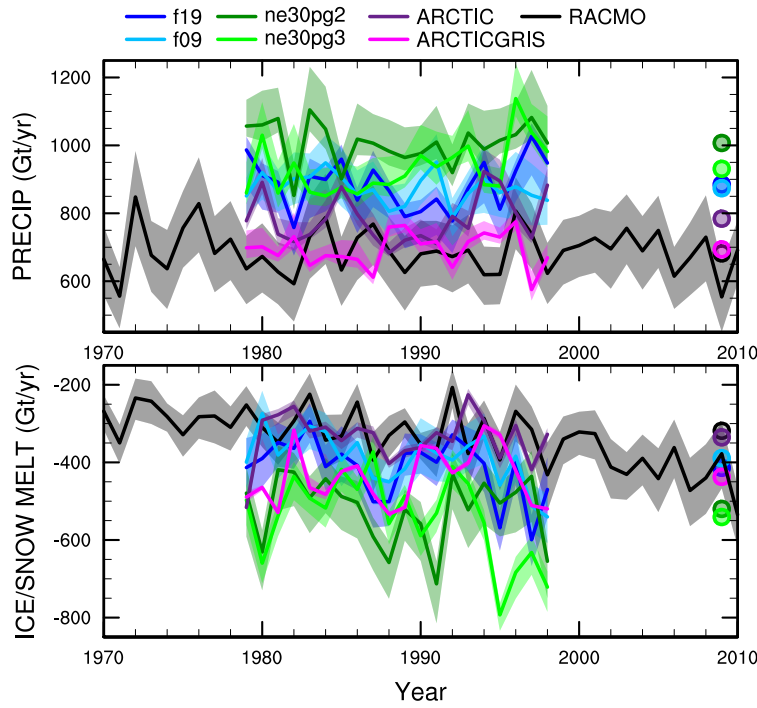


Figure 10. Time-series of annual (solid+liquid) precipitation (top) and annual runoff (bottom) integrated over the Greenland Ice Sheet for all six simulations and compared to the RACMO datasets. The time-series were generated using the common ice mask approach, which results in up to 4 ensembles, with the mean value given by the solid line and shading spanning the extent of the ensemble members.

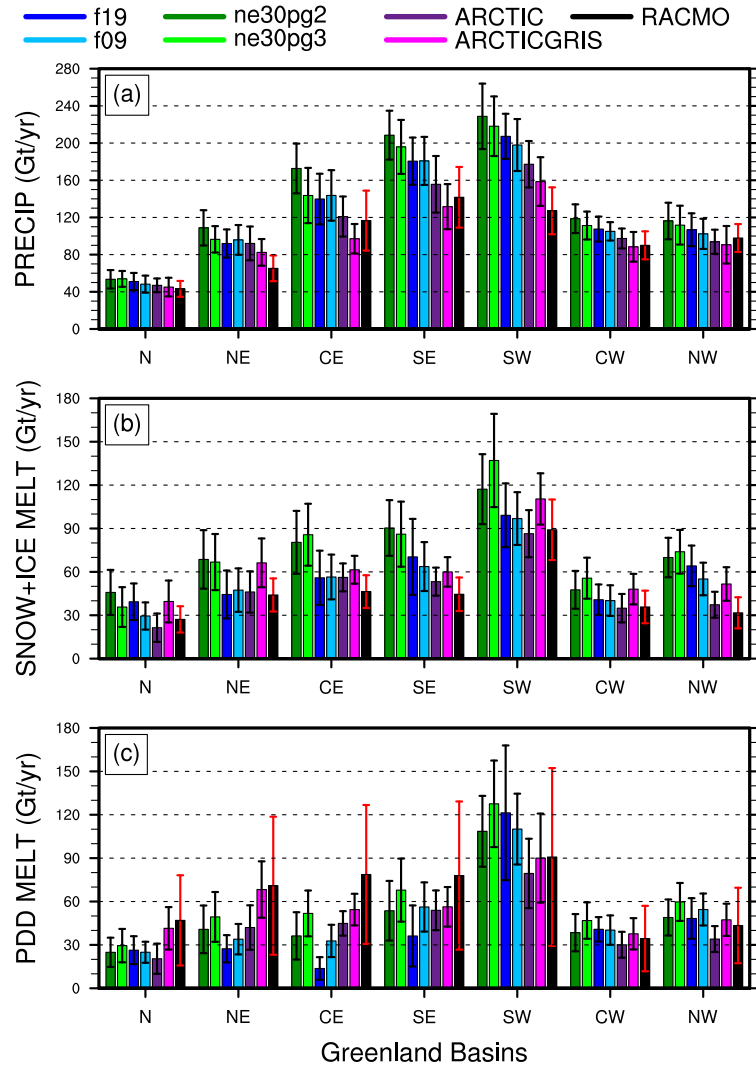


Figure 11. 1979–1998 basin integrated components of the SMB; (top) precipitation, (middle) ice/snow melt and (bottom) ice/snow melt estimated from the PDD method. Whiskers span the max/min of the four ensemble members generated from the common-ice-mask approach. Basin definitions are after Rignot and Mouginot (2012), and are found on the common ice masks using a nearest neighbor approach, and shown in Figure 9.

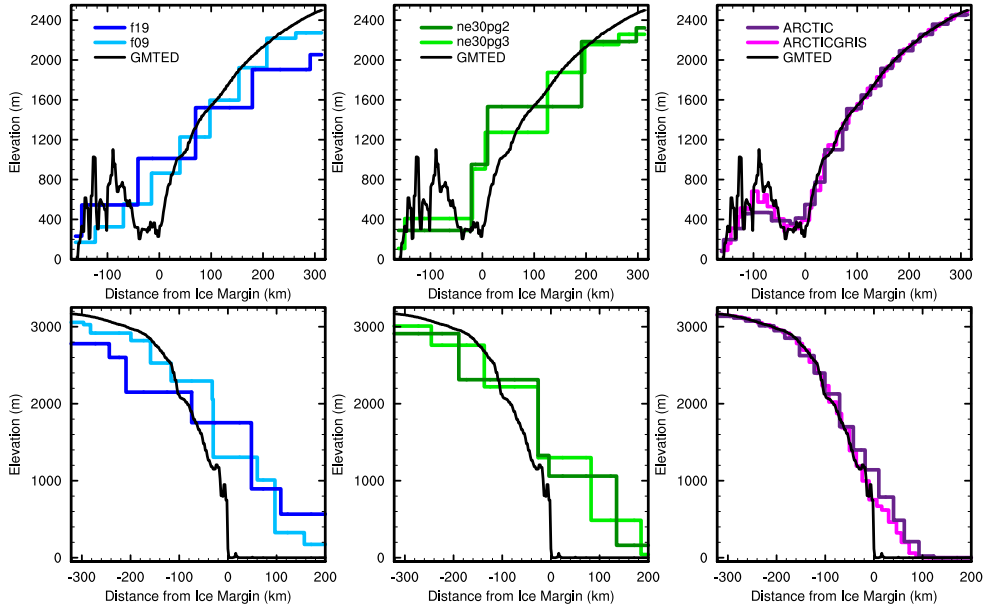


Figure 12. Model surface elevation along the (top) K-transect, and (bottom) a transect spanning the central dome down to the Kangerlussuaq glacier in southeast Greenland, for all model grids. The reference surface (GMTED) is a 1 km surface elevation dataset used for generating the CAM topographic boundary conditions.

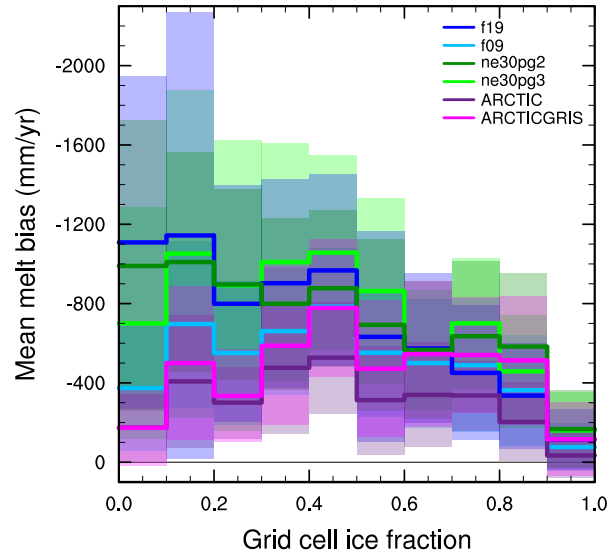


Figure 13. Fractional melt bias over the GrIS, computed relative to the RACMO datasets using the common ice mask approach, and conditionally sampled by grid cell ice fraction provided by the common ice masks. Solid lines are the mean of the distribution with \pm one standard deviation expressed by shading.

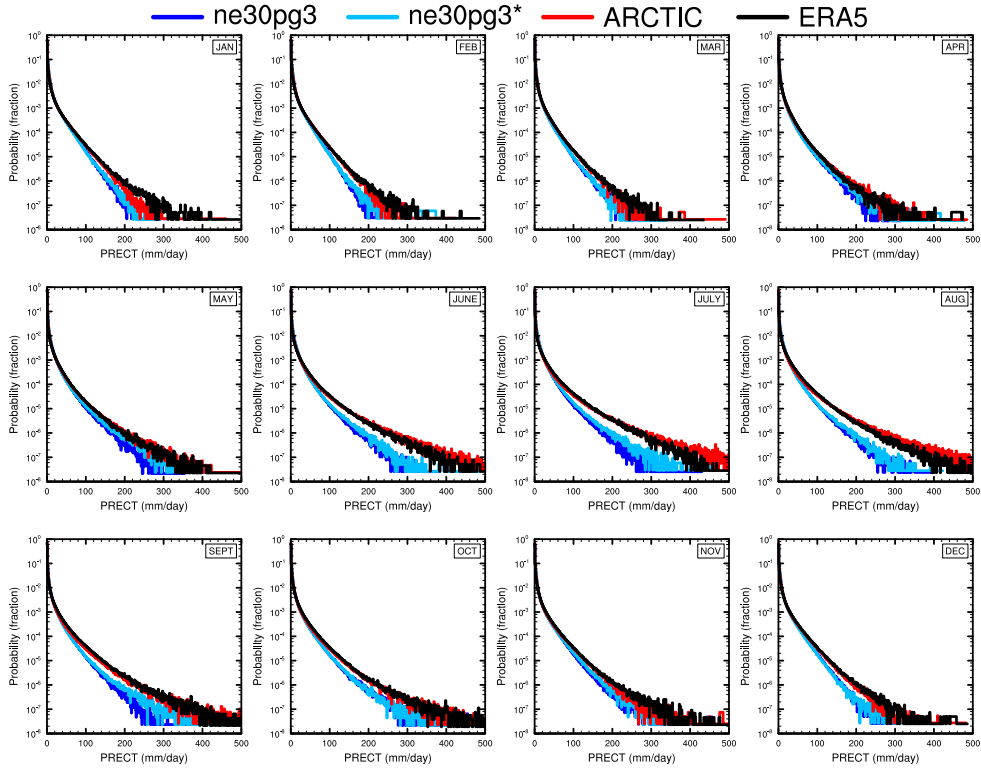


Figure 14. PDFs of the total precipitation rate associated with tracked storms, by month, in the ne30pg3, ne30pg3* and Arctic runs, and compared with the ERA5 dataset.

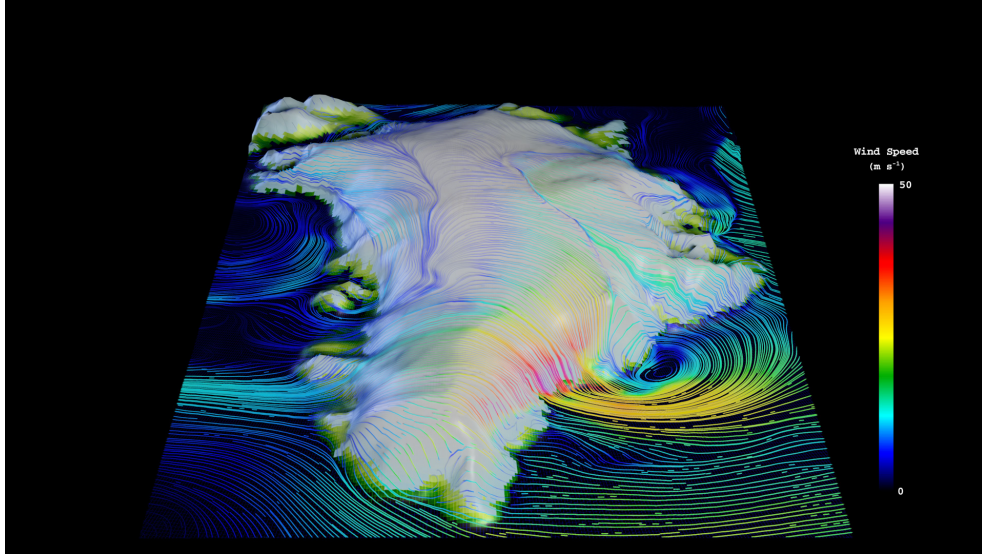


Figure 15. Snapshot of the lowest model level streamlines from the Arctic – GrIS visualization, with color shading denoting the wind magnitude.

OMEGA500, 1 year average, F2000climo, 32 levels

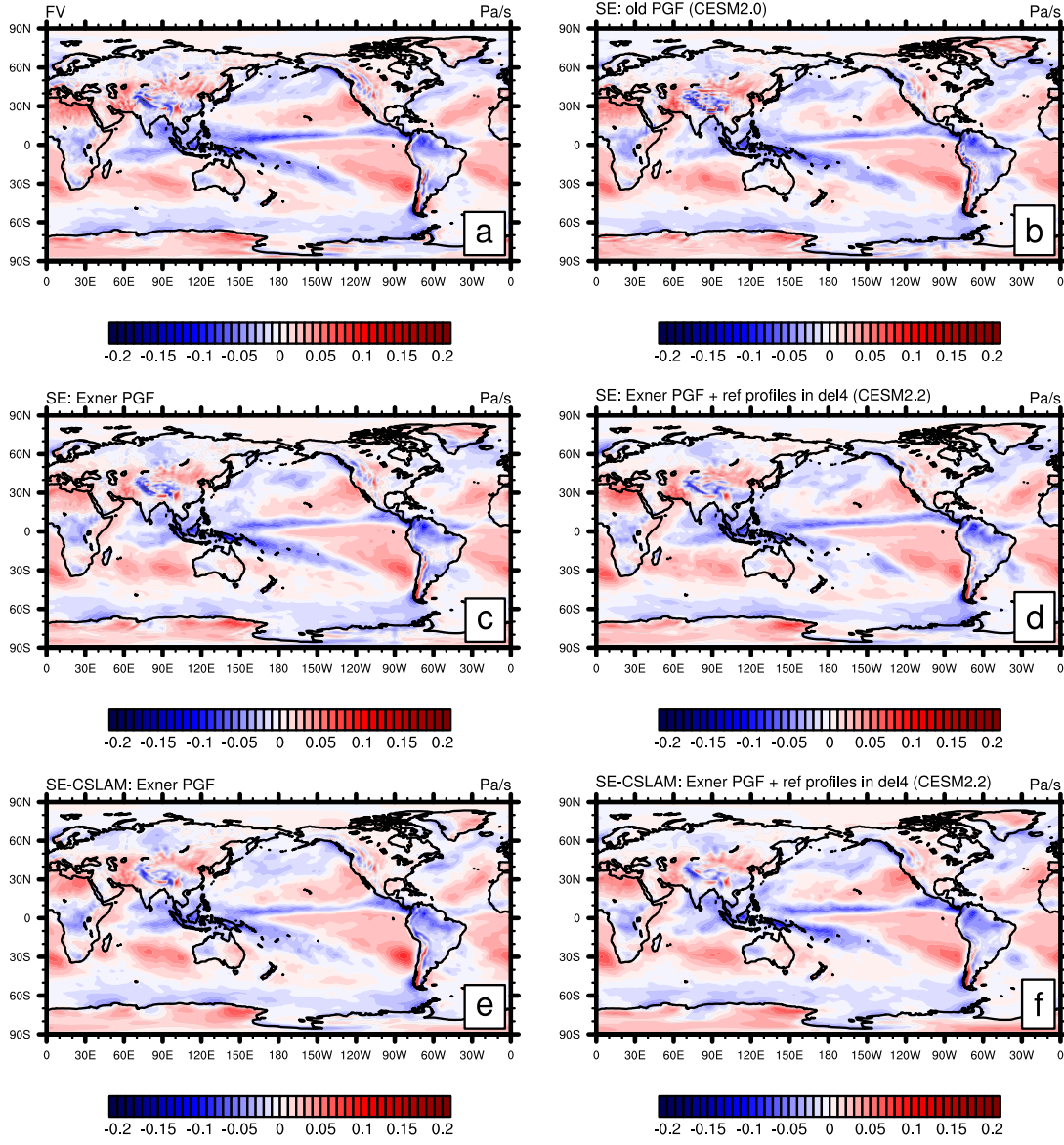


Figure A1. One year averages of vertical pressure velocity at 500hPa (OMEGA500) using (a) CAM-FV (Finite-Volume dynamical core) and (b-f) various versions of the spectral-element (SE) dynamical core at approximately 1° horizontal resolution and using 32 levels. (b) is equivalent to the CESM2.0 version of the SE dynamical core using the "traditional"/"old" discretization of the pressure-gradient force (PGF). Plot (c) is equivalent to configuration (b) but using the Exner form of the PGF. Plot (d) is the same as configuration (c) but also subtracting reference profiles from pressure and temperature before applying hyperviscosity operators (which is equivalent to the CESM2.2 version of SE in terms of the dynamical core). Plots (e) and (f) are equivalent to (c) and (d), respectively, by using the SE-CSLAM (`ne30pg3`) version of the SE dynamical core (i.e. separate quasi-uniform physics grid and CSLAM transport scheme).

OMEGA500, 18 months average, FHS94 forcing, 32 levels

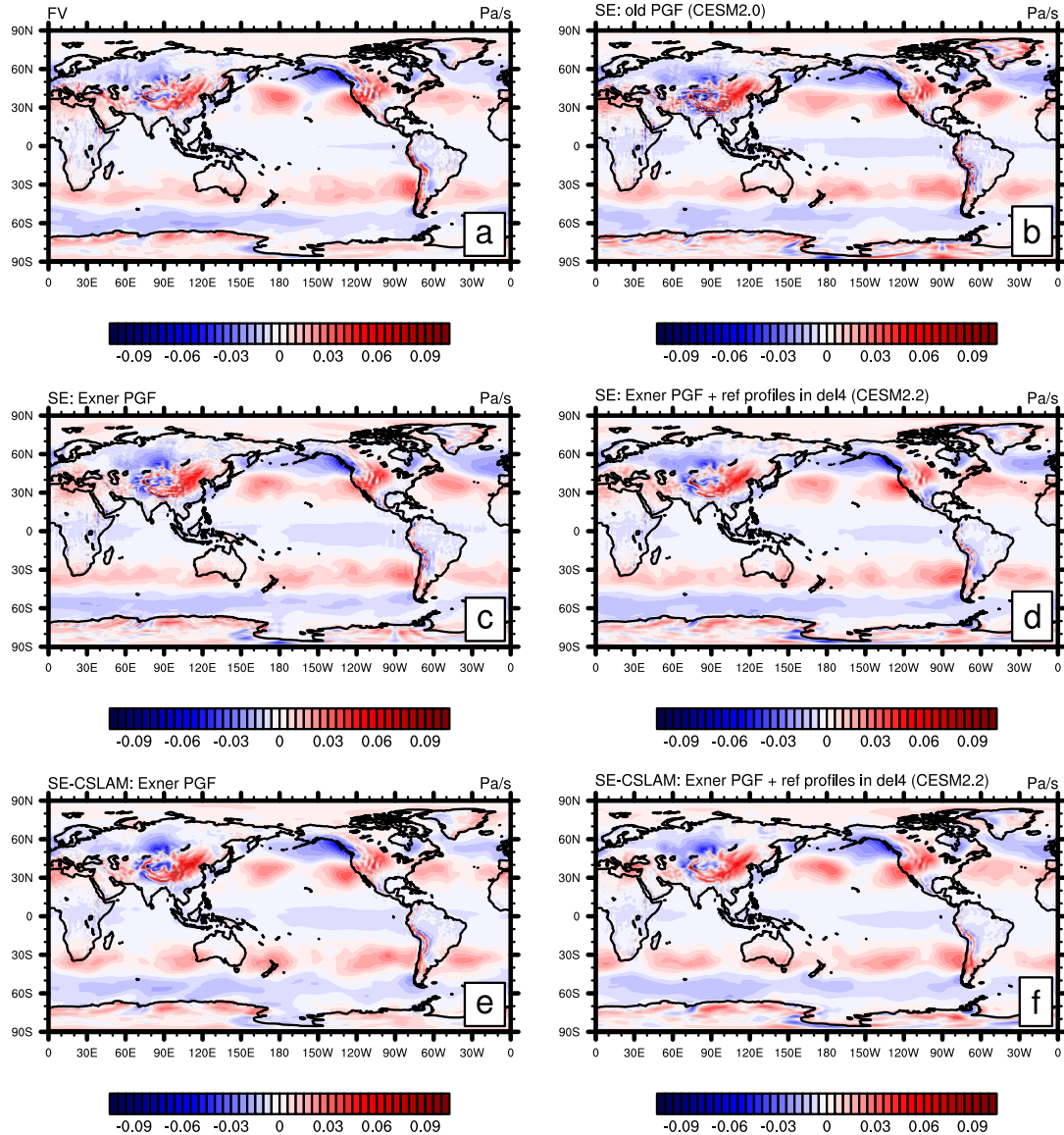


Figure A2. Same as Figure A1 but using modified Held-Suarez forcing and the average is over 18 months (excl. spin-up).